Cell Reports

Article

Movement-specific signaling is differentially distributed across motor cortex layer 5 projection neuron classes

Graphical abstract

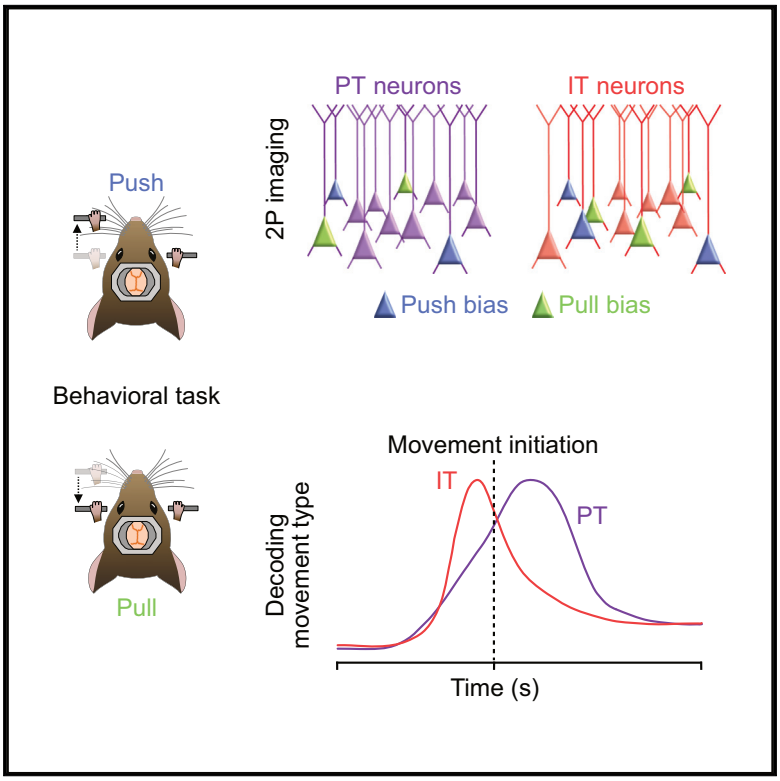

Authors

Stephen P. Currie, Julian J. Ammer, Brian Premchand, ..., A. Aldo Faisal, Matthias H. Hennig, Ian Duguid

Correspondence

ian.duguid@ed.ac.uk

In brief

Currie et al. show that movement-type-specific information is routed through relatively small, distributed subpopulations of motor cortical layer 5B projection neurons. Using 2-photon population calcium imaging, they demonstrate that movement-invariant signaling dominates layer 5B population dynamics, whereas movement-specific signaling is differentially distributed across projection neuron classes.

Highlights

- Movement-invariant responses dominate layer 5B population dynamics
- Small proportions of layer 5B projection neurons display movement-specific activity
- Movement specificity is differentially distributed across projection neuron classes
- IT neurons encode movement type before and PT neurons after movement initiation

Currie et al., 2022, Cell Reports *39*, 110801
May 10, 2022
https://doi.org/10.1016/j.celrep.2022.110801

CellPress

Cell Reports

CellPress
OPEN ACCESS

Article

Movement-specific signaling is differentially distributed across motor cortex layer 5 projection neuron classes

Stephen P. Currie,[1,9] Julian J. Ammer,[1,7,9] Brian Premchand,[1,8,9] Joshua Dacre,[1,9] Yufei Wu,[3] Constantinos Eleftheriou,[1,2] Matt Colligan,[1] Thomas Clarke,[1] Leah Mitchell,[1] A. Aldo Faisal,[3,4,5] Matthias H. Hennig,[6] and Ian Duguid[1,2,10,*]

[1]Centre for Discovery Brain Sciences and Patrick Wild Centre, Edinburgh Medical School: Biomedical Sciences, University of Edinburgh, Hugh Robson Building, George Square, Edinburgh EH8 9XD, UK
[2]Simons Initiative for the Developing Brain, Edinburgh Medical School: Biomedical Sciences, University of Edinburgh, Edinburgh EH8 9XD, UK
[3]Department of Bioengineering, Imperial College London, London SW7 2AZ, UK
[4]Department of Computing, Imperial College London, London SW7 2AZ, UK
[5]MRC London Institute of Medical Sciences, London W12 0NN, UK
[6]Institute for Adaptive and Neural Computation, School of Informatics, University of Edinburgh, Edinburgh EH8 9AB, UK
[7]Present address: Optophysiology, Faculty of Biology, University of Freiburg, 79100 Freiburg, Germany
[8]Present address: Infocomm Research, A*STAR, 1 Fusionopolis Way, #21-01 Connexis (South Tower), Singapore 138632, Singapore
[9]These authors contributed equally
[10]Lead contact
*Correspondence: ian.duguid@ed.ac.uk
https://doi.org/10.1016/j.celrep.2022.110801

SUMMARY

Motor cortex generates descending output necessary for executing a wide range of limb movements. Although movement-related activity has been described throughout motor cortex, the spatiotemporal organization of movement-specific signaling in deep layers remains largely unknown. Here we record layer 5B population dynamics in the caudal forelimb area of motor cortex while mice perform a forelimb push/pull task and find that most neurons show movement-invariant responses, with a minority displaying movement specificity. Using cell-type-specific imaging, we identify that invariant responses dominate pyramidal tract (PT) neuron activity, with a small subpopulation representing movement type, whereas a larger proportion of intratelencephalic (IT) neurons display movement-type-specific signaling. The proportion of IT neurons decoding movement-type peaks prior to movement initiation, whereas for PT neurons, this occurs during movement execution. Our data suggest that layer 5B population dynamics largely reflect movement-invariant signaling, with information related to movement-type being routed through relatively small, distributed subpopulations of projection neurons.

INTRODUCTION

In mammals, descending cortical output is necessary for the learning and execution of voluntary movements (Guo et al., 2015; Hwang et al., 2019, 2021; Kawai et al., 2015; Lawrence and Kuypers, 1968; Martin and Ghez, 1991). Deep-layer projections from primary motor cortex form multiple descending pathways innervating cortical, subcortical, brain stem, and spinal cord circuits necessary for triggering and controlling movement (for reviews, see Lemon, 2008; Ruder and Arber, 2019; Shepherd, 2013). Individual layer 5 projection neurons display complex firing patterns that correlate with various aspects of limb trajectories, such as joint angle, direction, and speed (Georgopoulos et al., 1982; Moran and Schwartz, 1999; Paninski et al., 2004; Thach, 1978), and during single-action tasks in rodents, most layer 5 projection neurons (>70%) display movement-related activity in the form of bidirectional changes in firing rate (Dacre et al., 2021; Estebanez et al., 2017; Levy et al., 2020; Park et al., 2022; Sauerbrei et al., 2019; Wang et al., 2017), suggesting widespread encoding of movement. However, in non-human primates, the largest components of motor cortex population responses during a delayed-multi-direction reach task have been shown to be "condition invariant," meaning the population response magnitude and time course were similarly irrespective of reach direction (Kaufman et al., 2016). Condition-invariant responses are tightly linked to the onset of movement, likely reflecting movement timing rather than movement type, similar to condition-invariant population transitions observed in recurrent neural networks trained to recapitulate complex muscle patterns in reaching primates (Sussillo et al., 2015). Deciphering how condition-invariant (which we call "movement-invariant") and movement-specific signaling is spatiotemporally organized in the output layers of motor cortex and how they map onto specific projection classes would be an important step toward understanding descending cortical control of movement.

In rodents, descending information from the main output layer of motor cortex, layer 5B, is routed via two molecularly and anatomically defined projection pathways. Pyramidal tract (PT) neurons innervate multiple targets, including the thalamus, subthalamic nucleus, superior colliculus, ipsilateral striatum, brain stem, and spinal cord, but not the cortex or contralateral striatum (Economo et al., 2018; Kita and Kita, 2012; Muñoz-Castañeda et al., 2021; Ueta et al., 2014; Winnubst et al., 2019), whereas intratelencephalic (IT) neurons target cortex and the striatum bilaterally but not other subcortical targets (Levesque et al., 1996; Muñoz-Castañeda et al., 2021; Wilson, 1987; Winnubst et al., 2019). Although layer 5B neurons are reciprocally connected (Kiritani et al., 2012; Morishima and Kawaguchi, 2006; Morishima et al., 2011), connectivity is essentially unidirectional from IT to PT neurons (Kiritani et al., 2012). This form of asymmetric across-projection class connectivity appears to be a common cortical motif necessary for sensorimotor processing (Brown and Hestrin, 2009; Kiritani et al., 2012; Molyneaux et al., 2007; Reiner et al., 2010). From a descending control perspective, asymmetric connectivity coupled with differential PT and IT intrinsic excitability, sensitivity to neuromodulation and local- and long-range inputs (for reviews, see Baker et al., 2018; Shepherd, 2013) provides a mechanism for flexible routing of information via distinct output channels depending on behavioral state and task requirements. Accumulating evidence suggests that PT neurons provide an essential source of descending control for execution of voluntary limb movements (Economo et al., 2018; Nelson et al., 2021; Peters et al., 2017; Soma et al., 2017; Wang et al., 2017), whereas IT neurons provide input to cortical and striatal circuits contributing to movement preparation and specification (Panigrahi et al., 2015; Park et al., 2022; Yttri and Dudman, 2016), but how movement-specific information is spatiotemporally organized across the two output channels remains unclear.

Here we performed 2-photon calcium imaging in deep layers of the caudal forelimb area (CFA) of mice trained to perform two diametrically opposing forelimb movements (i.e., an alternating push/pull lever task). By combining population imaging with neural classifiers and dimensionality reduction, we show that the majority of layer 5B neurons display movement-invariant signaling (i.e., the same magnitude of response for push and pull movements), correlated with movement timing rather than movement type, whereas small subpopulations of PT and IT neurons convey movement-specific information. Decoding movement type was most prevalent prior to movement initiation in IT neurons and during movement execution in PT neurons, with neurons with high decoding accuracy from both projection classes being temporally uncorrelated and distributed across layer 5B. These findings provide evidence that movement-invariant signaling dominates layer 5B activity, whereas movement-specific information is spatially and temporally distributed across projection neuron classes.

RESULTS

CFA is required for execution of a push/pull lever task for mice

To explore how layer 5B signaling relates to execution of different movements, we first developed a cued linear push/pull lever task for mice. The task design required mice to push or pull a horizontal lever during presentation of a 2-s 6 kHz auditory cue to receive a water reward. After a 4- to 6-s inter-trial interval (ITI), mice had to push the lever 4 mm forward from an initial starting position. The lever would then be locked, and a servo-controlled lick spout would deliver a 5-μL reward following a 1-s delay. The lever then unlocked, and a second ITI commenced, where mice would be expected to pull the lever backward 4 mm to the original starting position after presentation of the same 6-kHz auditory cue. Missed trials or spontaneous movement during the ITI resulted in a lever reset and restarting of the ITI (Figure 1A). Individual mice displayed idiosyncratic strategies to engage with the lever but showed reproducible trial-to-trial forelimb trajectories (Figure 1B). In general, mice reoriented their forelimb and paw upon cue presentation (lift and rotate backward for pushes, lift and rotate forward for pulls) (Video S1) prior to initiation of the push or pull action. Mice rapidly learned the task (mean, 10.5 days; [4] inter-quartile range (IQR); N = 24 mice), displaying fast reaction times and movement durations that reflect the combination of paw reorientation and lever manipulation (Figure 1C). "Expert" mice completed 44.5 [9.5] IQR successful push and 45.0 [8.5] IQR successful pull trials during each 30-min behavioral session, equating to ~71% task success (push median 68.0%, [35.9] IQR; pull median 74.5%, [43.4] IQR; N = 24 mice) (Figures 1D and 1E).

To confirm that CFA is required for execution of push and pull movements, we focally injected the Gamma aminobutyric acid type A ($GABA_A$) receptor agonist muscimol (1.6 mm lateral and 0.6 mm rostral of bregma; STAR Methods; Dacre et al., 2021; Schiemann et al., 2015). By applying muscimol during behavior, we could assess the immediate effects of CFA inactivation within the first 10 min after drug injection (Figure 1F), where drug diffusion remained in the targeted region (Figures S1A–S1C). Muscimol rapidly blocked initiation of both actions, reducing the number of successful trials in the first 10 min by ~65% (push Pre 13.9 [11.1 17.1] 95% CI trials, push Post 5.0 [3.3 6.8] 95% CI trials, N = 10 mice; pull Pre 14.0 [10.9 17.2] 95% CI trials, pull Post 5.3 [3.2 7.4] 95% confidence interval [CI] trials, N = 10 mice) (Figure 1G). Sham injections of saline into CFA or muscimol injections into hindlimb motor cortex had no effect on behavior (Figures S1D–1G). Blocking CFA activity resulted in an inability to initiate push or pull movements and monoparesis of the contralateral forelimb (i.e., localized weakness without complete loss of function), as evidenced by a significant reduction in paw position accuracy (i.e., the forepaw was not positioned on the lever at cue presentation) (Figures 1H and S1H–1J; Video S2). The effect of muscimol inactivation was most pronounced in mice that displayed the highest number of successful trials, confirming that task execution is CFA dependent even in expert mice (Hwang et al., 2019, 2021; Kawai et al., 2015; Figure S1K).

Movement-invariant signaling dominates layer 5B activity patterns

To examine how output from CFA relates to execution of push and pull movements, we restricted imaging of behavior-related population activity to cortical depths corresponding to layer 5B, the upper boundary of which was identified by the presence of

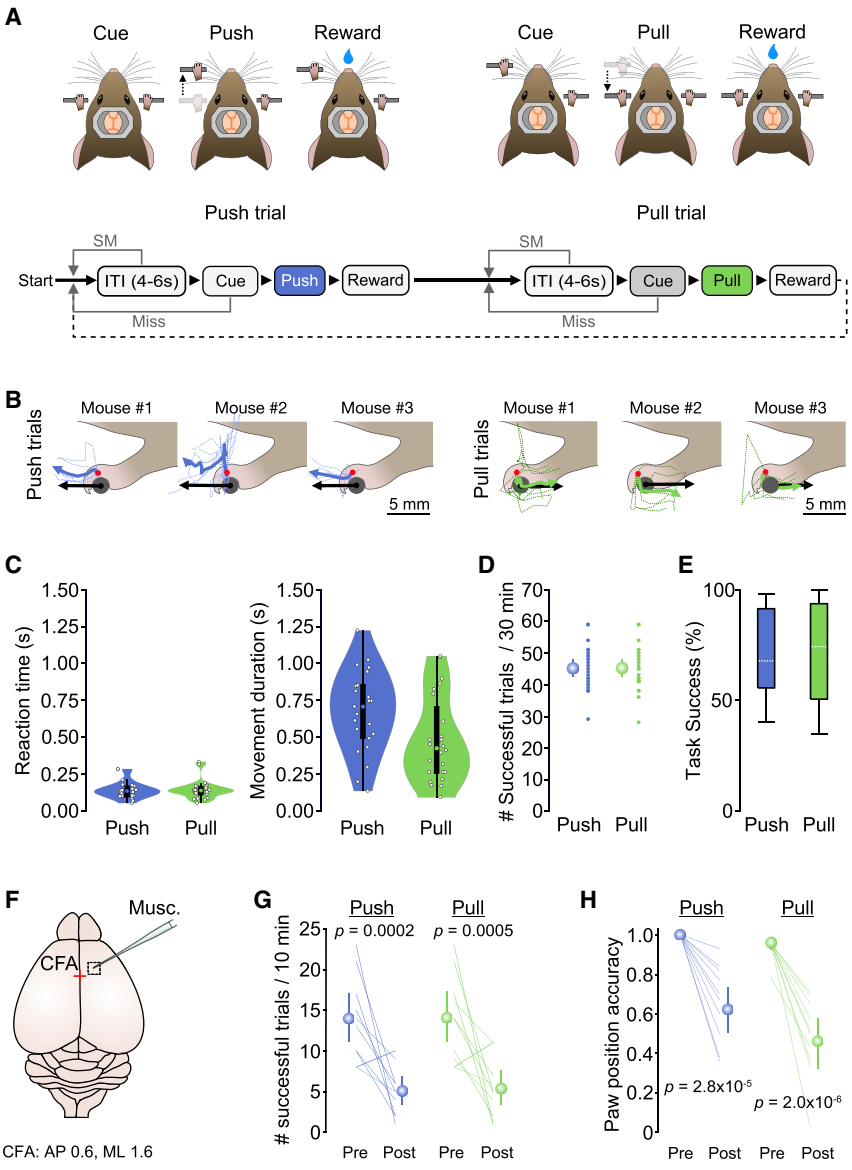

Figure 1. CFA is necessary for executing cued push and pull movements

(A) Top: cued alternating push/pull task for head-restrained mice. Bottom: behavioral task structure. ITI, inter-trial interval; SM, spontaneous movement.

(B) Paw and lever movement trajectories from 3 mice relative to position at movement initiation. Single trials (dashed lines) and mean paw trajectories (solid lines) during push (left, blue) and pull (right, green) trials are shown alongside the average movement vector of the lever (black arrow). Red dots depict approximate tracked positions on the paw.

(C) Violin plots showing median, IQR, and range of reaction times (left) and movement durations (right) during push (blue) and pull (green) trials. Circles represent data from individual mice (N = 24 mice).

(D) Number of successful trials per 30-min training session (small symbols, data from individual mice; large symbols, mean ± 95% CI; N = 24 mice).

(E) Box-and-whisker plots showing median, IQR, and range of task success across mice (N = 24 mice).

(F) Focal muscimol inactivation of CFA, centered 0.6 mm anterior and 1.6 mm medial of bregma (red cross).

(G) Number of successful push (blue) and pull (green) trials in a 10-min period before (Pre) and after (Post) injection of muscimol (N = 10 mice); paired t test. Colored lines, individual mice. Symbols, population means ± 95% CI.

(H) Paw position accuracy at the point of cue presentation before (Pre) and 10 min after (Post) muscimol injection into CFA (N = 10 mice); paired t test. Colored lines, individual mice. Symbols, population means ± 95% CI.

PT neurons in separate tracing experiments (CFA upper boundary ≥500 μm from the pial surface) (Schiemann et al., 2015; Figures 2A, 2B, and S2A). Cell density estimates suggested that we imaged the majority of layer 5B neurons at depths up to 650 μm from the pial surface (Figures S2A–2C). A large proportion of layer 5B neurons displayed movement-related activity (468 of 653 neurons, mean = 73.5% [54.7 81.8] 95% CI per field of view [FOV], N = 12 FOVs from 6 mice), defined as $\Delta F/F_0$ changes occurring within a peri-movement window spanning 150 ms prior to movement initiation to 40 ms after median movement completion. The remaining neurons were classified as non-responsive or reward-related when changes in $\Delta F/F_0$ occurred after the peri-movement window (Figures 2C and 2D). The trial-to-trial similarity in population responses of movement-related neurons strongly correlated with the similarity in forelimb movement magnitude (i.e., motion index; STAR Methods), suggesting that $\Delta F/F_0$ changes reflected movement of the forelimb (Figure 2E). By comparing push and pull trials, we found that most layer 5B neurons displayed movement-related activity that was indistinguishable between trial types (median = 59.8% [31.4] IQR of neurons, N = 6 mice), termed "movement-invariant" signaling, manifested as increased (85%) or decreased (15%) activity around movement onset. Movement-invariant neurons appeared to reflect the timing of movement (i.e., transition from a resting posture to push/pull) rather than movement type and were spatially distributed across each FOV (Figures 2F–2H). In contrast, only a small fraction of neurons displayed movement-specific signaling, where $\Delta F/F_0$ changes were significantly different between push and pull trials (termed movement bias; push bias, median = 14.3% [15.9] IQR; pull bias, median = 11.8% [19.5] IQR, N = 6 mice) (Figure 2M). Responses of movement bias neurons were classified into four different types, including positive and negative changes in $\Delta F/F_0$, consistent with bidirectional movement-specific tuning of neural activity (Georgopoulos et al., 1982). Most movement-bias neurons were classified as type 1 (136/181 neurons, 75.1%, N = 6 mice), showing increased $\Delta F/F_0$ during

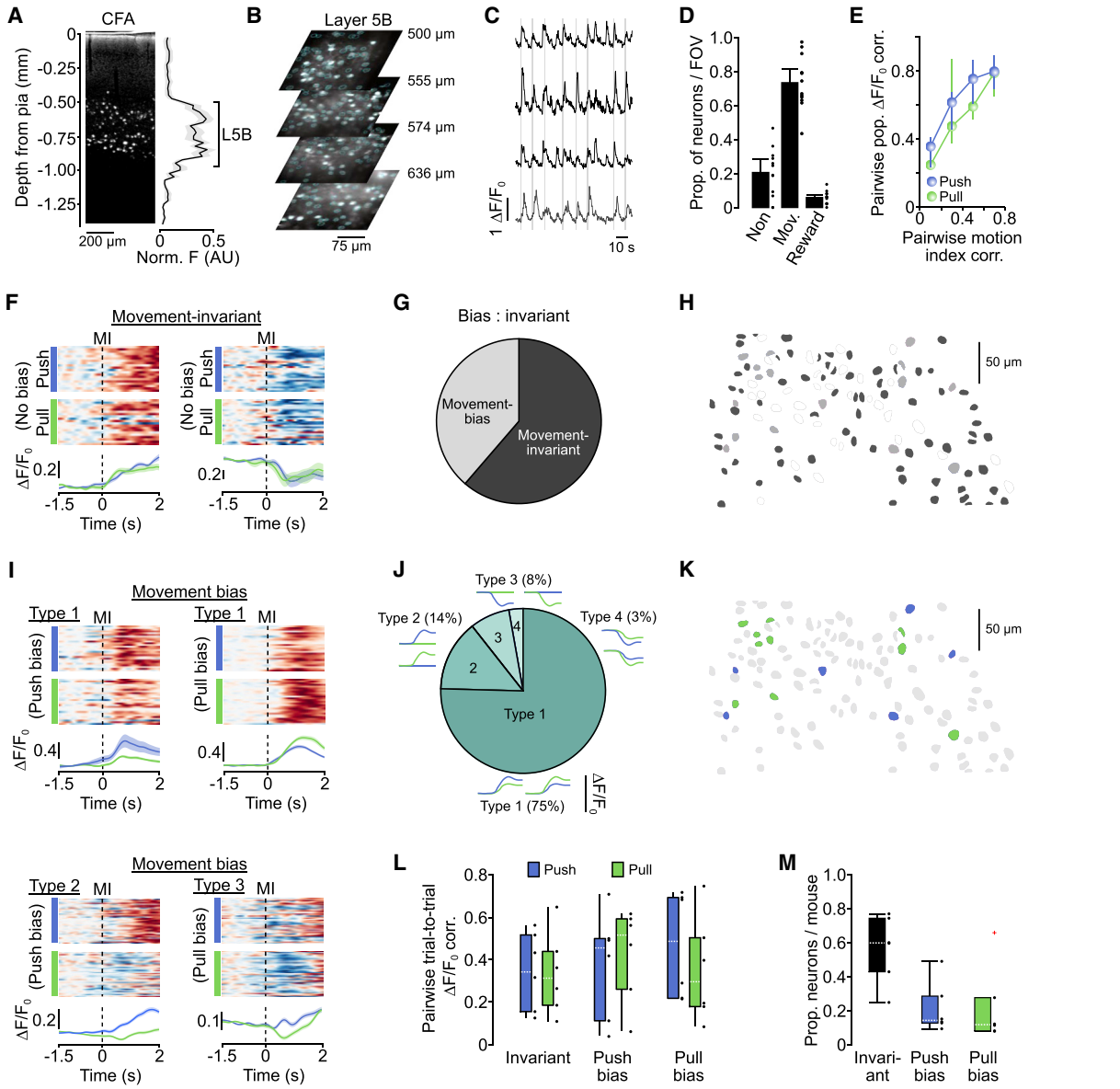

Figure 2. Movement-invariant and movement-specific signaling in layer 5B of CFA

(A) Depth profile of pyramidal tract (PT) neurons in CFA. Left: Retrobead labeling of PT neurons after injection into the pons. Right: normalized fluorescence ± SEM as a function of depth from the pial surface (N = 3 mice). A black line indicates the upper and lower boundary of layer 5B across mice.

(B) Representative 2-photon imaging fields of view (FOVs) from layer 5B in CFA (N = 4 mice). Cyan circles depict regions of interest.

(C) $\Delta F/F_0$ traces from four example layer 5B neurons during task execution (gray vertical bars). Black traces depict neurons with movement-related activity. Gray trace depicts a neuron with reward-related activity.

(D) Proportion of non-responsive, movement-related, or reward-related neurons per FOV (N = 12 FOVs from 6 mice). Black dots represent individual FOVs, and bars represent mean ± 95% CI.

(E) Pairwise trial-to-trial correlation of population $\Delta F/F_0$ during push (blue) or pull (green) trials as a function of the pairwise trial-to-trial correlation of the corresponding motion index (N = 12 FOV from 6 mice).

(F) Activity of two example movement-invariant neurons. Top: raster showing normalized $\Delta F/F_0$ across successive push (blue) or pull (green) trials. Bottom: mean $\Delta F/F_0$ ± 95% CI for push and pull trials. Dashed lines, movement initiation (MI).

(G) Summary of movement-invariant and movement-bias neuron classification in layer 5B of CFA (n = 468 neurons, N = 6 mice).

(H) 2 overlapping FOVs from a single mouse, showing movement-invariant (dark gray), movement bias (light gray), and non-responsive neurons (white).

(I) Activity of movement bias neurons split by type. Top: example type 1 neurons with push (left) or pull (right) bias. Bottom left: example type 2 neuron with push bias. Bottom right: example type 3 neuron with pull bias. Dashed lines, MI.

(J) Summary of movement bias classification in the layer 5B CFA (n = 181 neurons, N = 6 mice). Insets: model examples of type 1–4 $\Delta F/F_0$ changes.

(legend continued on next page)

push and pull trials, whereas smaller proportions of type 2 neurons (25/181 neurons, 13.8%, N = 6 mice) and type 3 (15/181 neurons, 8.3%, N = 6 mice) displayed movement selectivity (i.e., a significant change in $\Delta F/F_0$ for one movement with no response during the opposing movement). Finally, a small minority of cells displayed reduced activity during push and pull trials, classified as type 4 neurons (5 of 181 neurons, 2.8%; N = 6 mice) (Figures 2I and 2J). In terms of spatial organization, movement bias neurons were found in all FOVs and were spatially intermingled with movement-invariant neurons (Figures 2H and 2K). Although there was a high degree of variability in $\Delta F/F_0$ changes trial to trial, no consistent differences in mean pairwise trial to trial $\Delta F/F_0$ correlations were found between movement-invariant and movement-bias neurons across trial types (Figure 2L). A small proportion of bias neurons displayed differences in baseline $\Delta F/F_0$ between push and pull trials, which could reflect postural differences (i.e., different trial to trial start positions for push and pull trials) or differential preparatory activity (Li et al., 2015; Figures S2D–S2F). However, baseline differences were, on average, smaller than those observed during the peri-movement epoch (data not shown) and, thus, unlikely to be the main driver of movement-specific signaling. Given that $\Delta F/F_0$ changes provide an indirect readout of neural activity, we sought to confirm the proportions of movement-invariant and movement-bias neurons in layer 5B using high-density silicone probe recordings. Putative layer 5B projection neurons were identified using spike-width thresholding and electrode depth profiling based on retrograde labeling from the pons (Figures S2G–S2I). We found similar proportions of movement-invariant and push/pull bias neurons when comparing both recording methods (Figures 2M and S2J–S2L), confirming that movement-invariant signaling dominated layer 5B responses, whereas a small proportion of neurons conveyed movement-specific information.

Movement-specific signaling is more prevalent in superficial layers

Excitatory networks in primary motor cortex display a top-down laminar organization, where output from layer 2/3 provides strong excitatory input to upper layer 5B projection neurons (Anderson et al., 2010; Weiler et al., 2008). Thus, movement bias in layer 5B neurons could be inherited from top-down input. To explore this possibility, we imaged behavior-related activity in layer 2/3 of CFA and found that, in contrast to layer 5B, movement-specific signaling dominated, with ~60% of neurons displaying push or pull bias (movement bias, 216 of 375 neurons, 57.6%; movement-invariant, 159 of 375, 42.4%; N = 5 mice). The vast majority of movement bias neurons were classified as type 1 (200 of 216 neurons, 93.0%), showing increased $\Delta F/F_0$ during push and pull trials (Figures S3A–S3G). The difference in lamina-specific activity profiles could indicate a top-down convergence of movement-specific information where widespread movement bias signaling in layer 2/3 converges on specific subpopulations of downstream layer 5B neurons.

A small proportion of layer 5B neurons decode movement type

Next we investigated how reliably movement type could be decoded from layer 5B single-neuron and population changes in $\Delta F/F_0$ using a Gaussian naive Bayes classifier and logistic regression, respectively (STAR Methods). Approximately 37% of neurons (172 of 468 neurons) displayed decoding accuracy scores above chance (Figure 3A), similar to but slightly higher than the combined proportion of identified push and pull bias neurons (see Figure 2M), likely reflecting subtle differences in the sensitivity of both approaches (see also layer 2/3 decoding accuracy scores for comparison; Figure S3H). Given the trial-to-trial variability in $\Delta F/F_0$ and resultant moderate decoding scores (Figures 2I and 3A), we reasoned that population responses could provide a more robust movement-related signal that would enhance decoding of movement type. By applying logistic regression, population decoding was found to be consistently more accurate (single-cell median decoding accuracy = 0.61, [0.07] IQR; population median decoding accuracy 0.75, [0.16] IQR; N = 6 mice, $p = 2.8 \times 10^{-2}$, Wilcoxon signed rank test) (Figure 3B). However, this increase was driven almost entirely by a small proportion of neurons with high decoding accuracy. Removing the top ~20% of neurons ordered by decoding accuracy score abolished movement type classification (median prop. removed = 0.21, [0.50] IQR, N = 6 mice), whereas sequential removal of randomly selected neurons resulted in a significantly larger proportion of neurons having to be removed before decoding accuracy reduced to chance (median prop. removed = 0.64, [0.57] IQR, N = 6 mice, $p = 2.8 \times 10^{-2}$, Wilcoxon signed rank test) (Figure 3D–3F). This dependency on neurons with high decoding accuracy suggests that movement-specific information is routed through a selected subset of layer 5B neurons.

To further explore the underlying structure of layer 5B population activity, we employed principal-component analysis (Churchland et al., 2010, 2012; Cunningham and Yu, 2014; Kaufman et al., 2014; Stopfer et al., 2003). For the leading 16 principal components, we compared the difference between push and pull trials to compute a discrimination index (d') (Figure S4A). Leading principal components tended to be more similar across actions, whereas movement type was often better represented by higher components (Figure S4B). Despite correlating with population decoding scores, high d' values were not preferentially associated with the leading principal components of the population activity (Figures S4C–4E), suggesting that movement type is not a dominant signal in the population response (Kaufman et al., 2016).

(K) 2 overlapping FOVs from a single mouse, showing neurons with push (blue) or pull (green) bias. Gray, movement-invariant, non-responsive, or reward-phase neurons.

(L) Mean pairwise trial-to-trial $\Delta F/F_0$ correlation for push (blue) and pull (green) trials in invariant and push- and pull-biased neurons (n = 468 neurons from 12 FOVs, N = 6 mice). Black dots represent individual mice.

(M) Proportion of invariant and push- and pull-biased neurons per mouse (n = 468 neurons from 12 FOVs, N = 6 mice). Black dots represent individual mice. A red cross marks an identified outlier.

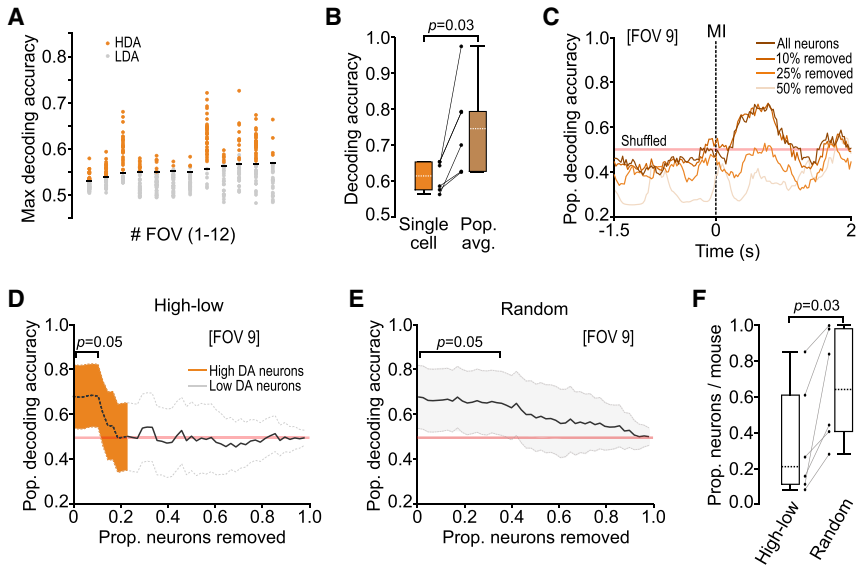

Figure 3. Population decoding relies on a small proportion of neurons with high decoding accuracy

(A) Maximum decoding accuracy during peri-movement epochs generated using a Gaussian naive Bayes classifier. Circles represent individual neurons; black horizontal lines indicate significance threshold. HDA, high decoding accuracy (orange); LDA, low decoding accuracy (gray).

(B) Box-and-whisker plots showing median, IQR, and range of single-cell (naive Bayes classifier, orange) and population (logistic regression, brown) decoding accuracy (N = 12 FOVs from 6 mice, p = 2.8×10^{-2}, Wilcoxon signed-rank test). Black dots represent individual mice.

(C) Mean population decoding accuracy for all neurons from a representative FOV (all neurons) or after removal of 10%–50% of neurons in order from high to low single-cell decoding accuracy (A). Red shaded line, 95% CI based on shuffled data. Dashed line, MI.

(D) Change in population decoding accuracy for an example FOV after sequential removal of neurons in order from high (orange) to low (gray) single-cell decoding accuracy (A). Line, mean ± 95% CI. Red line, 95% CI based on shuffled data.

(E) Change in population decoding accuracy for an example FOV after random removal of individual neurons. Line, mean ± 95% CI. Red line, 95% CI based on shuffled data.

(F) Box-and-whisker plots showing the median, IQR, and range for ordered (HDA to LDA) versus random removal of neurons (N = 12 FOVs from 6 mice, p = 2.8×10^{-2}, Wilcoxon signed-rank test). Black dots represent individual mice.

IT and PT neurons display temporal differences in encoding of movement type

Layer 5B contains two broad classes of projection neurons: IT neurons form striatal and cortico-cortical connections (Levesque et al., 1996; Muñoz-Castañeda et al., 2021; Wilson, 1987; Winnubst et al., 2019), whereas PT neurons target multiple subcortical, brain stem, and spinal cord areas (Economo et al., 2018; Kita and Kita, 2012; Muñoz-Castañeda et al., 2021; Ueta et al., 2014; Winnubst et al., 2019) (Figure 4A). We next sought to understand whether movement-specific and movement-invariant signaling was dependent on projection class identity. To perform population imaging from identified cell types, we used an intersectional retrograde viral approach targeting the ipsilateral brain stem (pons, PT) and contralateral CFA (IT) using a retrograde adeno-associated virus (r-AAV-retro cre) and conditional expression of GCaMP6s in ipsilateral CFA (Figures 4B and 4C). Using a bicistronic viral vector expressing GCaMP6s (flex) and mRuby, we confirmed that we recorded from the majority of PT and IT neurons per FOV at depths of up to 700 μm from the pial surface (Figure S5), consistent with our previous estimates (Figures S2A–2C). Comparing push and pull trials, most PT neurons displayed movement-invariant activity (75.0% [21.1] IQR), with a small number of neurons displaying push or pull bias (push bias = 10.3% [19.9] IQR, pull bias = 13.8% [11.3] IQR, N = 5 mice), mainly consisting of type 1 (78.2%) and type 2 neurons (16.9%) (Figures 4D and 4E). In contrast, similar proportions of IT neurons displayed movement-specific and movement-invariant signaling (movement bias = 48.8% [11.6] IQR), movement-invariant = 51.2% [11.6] IQR) with type 1 and type 2 neurons again being the most abundant (Figures 4F and 4G). Single-cell decoding accuracy scores were highly consistent across mice, and, as expected, population decoding accuracy increased when averaging the activity of all high-decoding-accuracy neurons per FOV (Figures 4H and 4I). Although trial type could only be decoded in approximately one-third of projection neurons during the peri-movement window, the proportion of IT neurons with decoding accuracy above chance was highest prior to movement initiation, whereas for PT neurons, this occurred during movement execution (IT peak proportion of neurons, 0.19 at −192 ms; PT peak proportion of neurons, 0.21 at +544 ms, N = 6 and 5 FOVs from 5 and 4 mice, respectively), suggesting differential roles for IT and PT populations in movement initiation and execution, respectively. Importantly, at no time during the peri-movement window was the proportion of neurons with high decoding accuracy above 21% for either cell type (Figure 4J), consistent with a small proportion of projection neurons conveying time-dependent, movement-specific information.

Movement-specific signaling is distributed across layer 5B

To explore whether high decoding accuracy PT and IT neurons form functional clusters, we first detected the onset of movement-related $\Delta F/F_0$ changes. Within each FOV, activity changes occurred ~300 ms prior to movement, consistent with a role in preparation/initiation (Dacre et al., 2021; Estebanez et al., 2017; Isomura et al., 2009; Li et al., 2015), and tiled the peri-movement window. Neurons displaying a range of $\Delta F/F_0$ onsets were spatially distributed across each FOV (Figures 5A and 5B). To explore correlations in peri-movement activity patterns, we split PT and IT neurons based on their decoding accuracy scores (high, low, and all) and compared pairwise activity during push

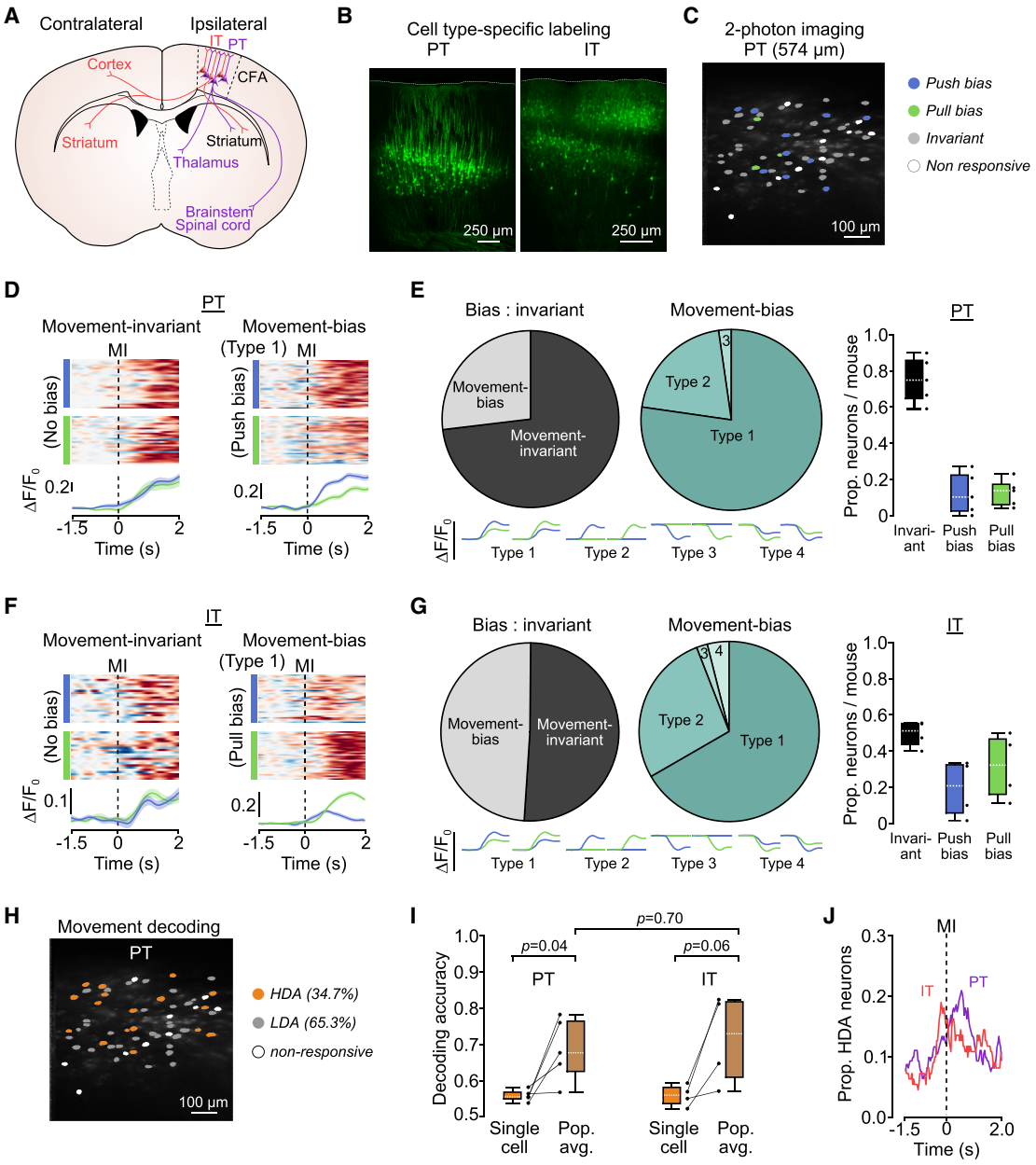

Figure 4. Movement-invariant and movement-specific signaling in identified layer 5B projection neurons

(A) Schematic showing brain-wide projections of layer 5B PT (purple) and IT (red) neurons. Contra- and ipsilateral relate to the site of 2-photon imaging.

(B) Histology from two imaged mice showing retrograde cell-type-specific labeling of PT (left) and IT (right) neurons in CFA.

(C) Example FOV showing PT neurons with push (blue) or pull (green) bias. Gray, movement invariant; white, non-responsive neurons.

(D) Activity of two example PT neurons: movement-invariant (left) and movement bias, type 1 (right). Top: raster showing normalized $\Delta F/F_0$ across successive push (blue) or pull (green) trials. Bottom: mean $\Delta F/F_0 \pm 95\%$ CI for push and pull trials. Dashed lines, MI.

(E) Left: summary of movement-invariant and movement bias PT neuron classification (n = 125 versus 46 neurons, N = 5 mice). Center: summary of movement bias classification in PT neurons (n = 46 neurons, N = 5 mice). Right: proportion of invariant, push- and pull-biased PT neurons per mouse (n = 171 neurons from 6 FOVs, N = 5 mice). Black dots represent individual mice. Bottom: model examples of $\Delta F/F_0$ changes classified as type 1–4.

(F) Activity of two example IT neurons: movement-invariant (left) and movement bias, type 1 (right). Top: raster showing normalized $\Delta F/F_0$ across successive push (blue) or pull (green) trials. Bottom: mean $\Delta F/F_0 \pm 95\%$ CI for push and pull trials. Dashed lines, MI.

(G) Left: summary of movement-invariant and movement bias IT neuron classification (n = 56 versus 54 neurons, N = 4 mice). Center: summary of movement bias classification in layer 5B IT neurons (n = 54 neurons, N = 4 mice). Right: proportion of invariant, push- and pull-biased layer 5B IT neurons per mouse (n = 110 neurons from 5 FOVs, N = 4 mice). Black dots represent individual mice. Bottom: model examples of $\Delta F/F_0$ changes classified as type 1–4.

(H) Example FOV showing HDA (orange), LDA (gray), and non-responsive (white) PT neurons.

(legend continued on next page)

and pull trials. We found weak correlations within and across groups irrespective of cell type identity (Figures 5C, 5D, and S6). Moreover, comparing the activities of PT and IT neurons as a function of their pairwise distance suggested that neighboring neurons did not show correlated activity or spatiotemporal clustering (Figures 5E–5G). Thus, our data suggest a model where movement-specific information is routed through small, distributed subpopulations of layer 5B projection neurons, whereas most neurons convey movement-invariant information related to the timing of movement execution (Figure 5H).

DISCUSSION

Here we have shown that layer 5B neuronal signaling is mostly movement-invariant, with similar activity patterns generated during execution of two diametrically opposing movements. Changes in activity were tightly locked to the peri-movement period, indicative of a generic motor signal relating to movement timing but not movement type. Movement- or condition-invariant signaling also dominates in primate motor cortex, thought to trigger state-dependent switching from stable neural dynamics during rest toward oscillatory dynamics underpinning movement execution (Churchland et al., 2010, 2012; Kaufman et al., 2014, 2016; Kurtzer et al., 2005), and is an emergent property of recurrent neural networks trained to recapitulate complex muscle patterns during reaching (Sussillo et al., 2015). In contrast to primate motor cortex, we found widespread movement-invariant responses at the single-neuron level (Kaufman et al., 2016). This is unlikely to reflect differences in recording sensitivity, given that our imaging and electrophysiology approaches identified similar proportions of movement-invariant neurons across layer 5B (Wei et al., 2020; Zhou and Tin, 2021), or the limited number of movements in our task because movement-invariant responses have been shown in relatively simple tasks requiring few actions (Evarts, 1968; Hocherman and Wise, 1991; Messier and Kalaska, 2000; Riehle et al., 1994; Weinrich et al., 1984) and in complex tasks involving more than 20 separate actions (Kaufman et al., 2016). Instead, this might reflect evolutionary differences in how motor cortex recruits and controls muscle activation during the transition from rest to movement execution. Cell-type-specific imaging identified that movement-invariant signaling dominated PT neuron activity, suggesting that a large proportion of the output conveyed to subcortical, brain stem, and spinal cord areas relates to execution of movement without necessarily specifying movement type, whereas equal proportions of IT neurons displayed movement-invariant versus movement-specific signaling. If movement-invariant signaling relates to the execution of movement and dominates deep-layer motor cortex activity, then what drives the change in neural activity, and what purpose might it serve? Long-range inputs from the thalamus, basal ganglia, secondary motor cortex, and cerebellum are possible sources (Hooks et al., 2013, 2018; Nelson et al., 2021), providing an external trigger to transform motor cortical dynamics necessary for postural maintenance at rest to a neural state required for movement execution. This switch in neural dynamics would signify the intention to move, but not which movement will be executed (Elsayed et al., 2016; Kaufman et al., 2016). An important next step will be to develop methods to identify and selectively manipulate neurons displaying movement-invariant signaling to demonstrate their causal contribution to postural control and timing of movement execution.

We reasoned that execution of two diametrically opposing movements should, in principle, generate distinct patterns of cortical output dynamics, given differences in starting posture, direction of movement, and temporal sequence of muscle activation (Isomura et al., 2009; Miri et al., 2017). Although we found that the majority of layer 5B neuron signaling was movement invariant, a relatively small proportion of neurons displayed response bias toward push or pull movements. The relatively low level of movement-specific signaling is unlikely to be due to masking of subtle changes in spike rate when using calcium reporters (Wei et al., 2020; Zhou and Tin, 2021) because we observed similar proportions of movement-specific signaling when performing high-density extracellular recordings of putative layer 5B projection neurons. The firing rates of individual neurons in motor cortex reflect a complex combination of signals that correlate with joint angle, direction, and speed (Georgopoulos et al., 1982; Moran and Schwartz, 1999; Paninski et al., 2004; Thach, 1978), whereas population dynamics reflect time-varying changes in neural state during the transition from rest to movement execution (Churchland et al., 2010, 2012; Kaufman et al., 2014, 2016; Kurtzer et al., 2005; Sauerbrei et al., 2019). In mice, individual layer 5B neurons displayed moderate decoding accuracy scores, likely because of relatively high trial-to-trial variability, whereas the population average was consistently higher across mice. We found that only a small proportion ($\sim$20%) of neurons contributed to high population decoding accuracy scores, with their combined effects accurately decoding three-quarters of all trials. Removing only a handful of neurons per FOV was sufficient to abolish decoding, confirming that a minority of neurons convey the majority of information regarding movement type. This dependency on only a few neurons has important implications for understanding how movement-specific information is encoded in primary motor cortex, given that recording of neural dynamics during execution of a single movement task will likely uncover widespread movement-invariant signaling, which relates to limb movement, but not the specific movement being executed.

In mouse cortex, projection neurons display connectivity patterns within and across classes that suggest general organizing principles (Brown and Hestrin, 2009; Kiritani et al., 2012; Maruoka et al., 2017; Morishima et al., 2011). IT neurons in motor cortex are strongly recurrently connected, whereas inter-class connectivity is largely directional from IT to PT but not vice versa, generating a hierarchical organization with unidirectional signaling from higher-order to lower-order output neurons

(I) Box-and-whisker plots showing median, IQR, and range of single-cell (naive Bayes classifier, orange) and population (logistic regression, brown) decoding accuracy of PT (left) and IT (right) neurons. Comparisons were made with a two sample t test. Black dots represent individual mice.
(J) Proportion of neurons with decoding accuracy above chance (i.e., HDA) across time. PT, purple; n = 58/171 neurons from 6 FOVs, N = 5 mice. IT, red; n = 43/110 neurons from 5 FOVs, N = 4 mice. Dashed line, MI.

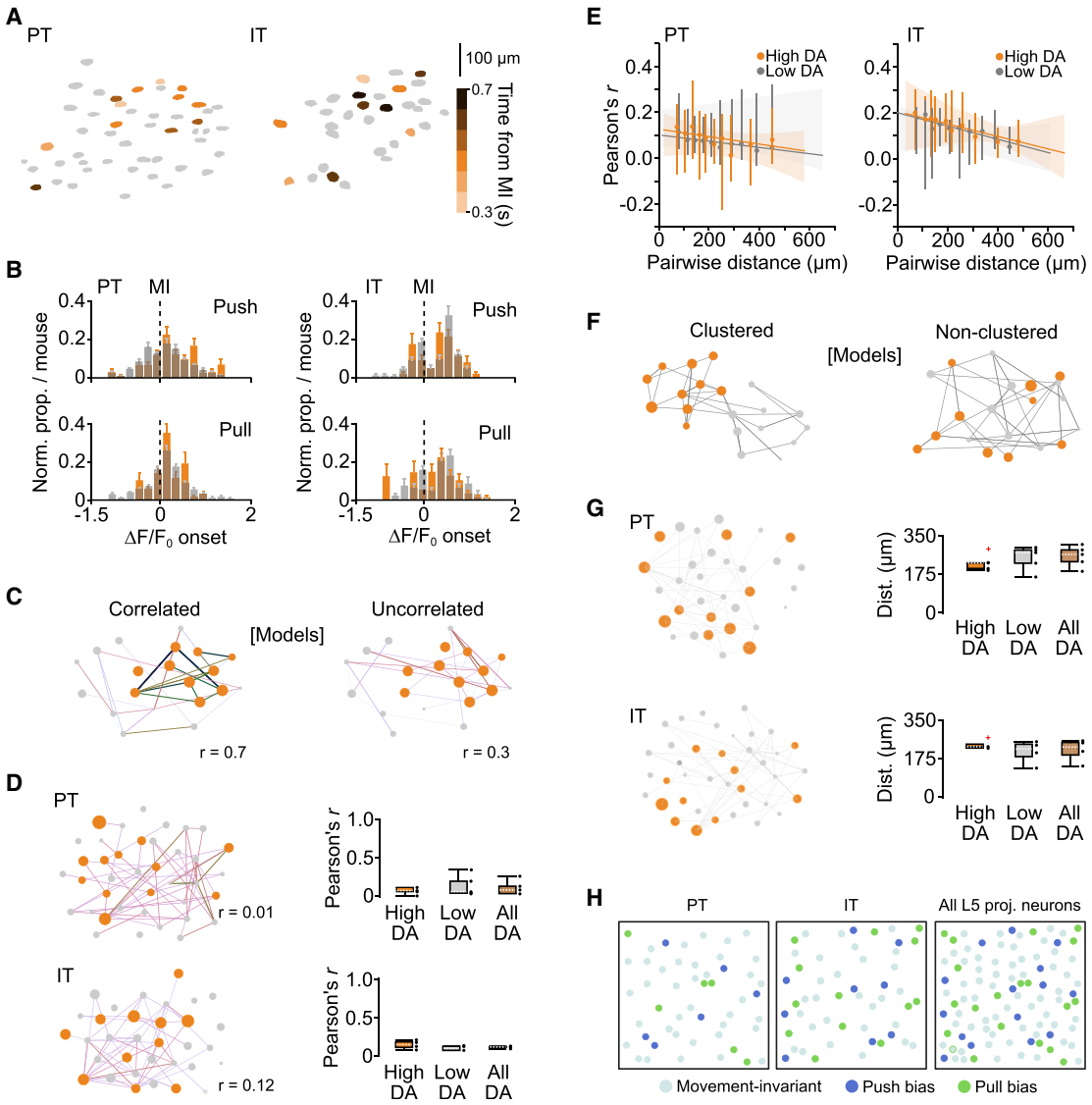

Figure 5. Cell-type-specific spatiotemporal organization of HDA neurons in layer 5B

(A) Example FOVs showing spatial distribution of $\Delta F/F_0$ onset for HDA PT (left) and IT (right) neurons during push trials. Colors represent 200-ms bins tiling the peri-movement epoch: −300 ms (light orange) to +700 ms (dark brown).

(B) Histograms of $\Delta F/F_0$ onset for HDA (orange) and LDA (gray) PT (left) and IT (right) neurons during push (top) and pull (bottom) trials (n = 6 and 5 FOVs, N = 5 and 4 mice, respectively).

(C) Modeled functional networks depicting HDA (orange) and LDA (gray) neurons with correlated (left) or uncorrelated (right) activity. Each node, represented by a circle, corresponds to a neuron, whereas the connections represent the strength of activity correlation between neurons.

(D) Left top and bottom: functional networks constructed from the pairwise activity correlations from a representative PT (top) and IT (bottom) FOV. Line color (light to dark) and width correspond to increasing values of Pearson's r. Neurons are plotted as nodes in Euclidean space, with color and size relating to increasing decoding accuracy. Right top and bottom, box-and-whisker plots showing the median, IQR, and range of correlation coefficients across mice for HDA (orange), LDA (gray), and all (brown) PT (top) and IT (bottom) neurons. Black dots represent individual mice.

(E) Median pairwise correlation coefficient with 95% CI as a function of pairwise distance for HDA (orange) and LDA (gray) PT (left) and IT (right) neurons. Horizontal lines denote linear regression model fit, with shaded regions representing the bootstrapped 95% CI (PT: p = 0.87 [(HDA], p = 1.0 [LDA], n = 3,024 observations, N = 5 mice; IT: p = 0.6 [HDA], p = 1.0 [LDA], n = 1,562 observations, N = 4 mice).

(F) Modeled functional networks depicting clustered (left) and non-clustered (right) HDA neurons. Each node, represented by a circle, corresponds to a neuron, whereas the connections represent the pairwise distances between neurons.

(G) Left top and bottom: functional networks constructed from the pairwise distances between neurons in a representative PT (top) and IT (bottom) FOV. Right top and bottom: box-and- whisker plots showing the median, IQR, and range of median pairwise distances across mice for HDA (orange), LDA (gray), and all (brown) PT (top) and IT (bottom) neurons. Black dots represent pairwise distances for individual mice, and red crosses mark identified outliers.

(H) Models depicting cell-type- and movement-specific layer 5B signaling in caudal forelimb area of motor cortex (CFA). Colored circles represent movement-invariant (cyan), push bias (blue), and pull bias (green) neurons.

(Kiritani et al., 2012). Asymmetric projection-class connectivity as well as differences in input structure and intrinsic excitability (Anderson et al., 2010; Hooks et al., 2013; Kiritani et al., 2012; Oswald et al., 2013) provide a mechanism to flexibly route movement-specific information via two independent output channels depending on behavioral requirements. Our cell-type-specific imaging identified that only a small proportion of PT neurons conveyed movement-specific information. In contrast, almost half of IT neurons displayed movement specificity, with similar proportions of push and pull bias. Although PT and IT activity onsets occurred prior to and throughout movement, consistent with both pathways contributing to movement initiation and execution (Chen et al., 2017; Economo et al., 2018; Li et al., 2015; Park et al., 2022; Wang et al., 2017), the proportion of IT neurons with high decoding accuracy was highest prior to movement initiation, whereas for PT neurons, this occurred during movement execution. This suggests that information relating to movement type is first conveyed by IT neurons, which project to the cortex and bilaterally to the striatum but not other subcortical structures (Levesque et al., 1996; Muñoz-Castañeda et al., 2021; Wilson, 1987; Winnubst et al., 2019), before PT neurons then propagate information to subcortical, brain stem, and spinal cord circuits necessary for online control of forelimb movement (Economo et al., 2018; Kita and Kita, 2012; Muñoz-Castañeda et al., 2021; Ueta et al., 2014; Winnubst et al., 2019). Importantly, the proportions of PT or IT neurons decoding movement type at any time never exceeded 25%, consistent with movement-specific signaling being confined to a relatively small subpopulation of layer 5B projection neurons. What is unclear is the extent to which movement-specific signaling in PT and IT neurons is organized by the projection target, as seen in anterolateral motor cortex during directional licking (Chen et al., 2017; Economo et al., 2018; Li et al., 2015). Targeting neurons based on molecular expression profiles and projection specificity (Muñoz-Castañeda et al., 2021; Winnubst et al., 2019) will provide a finer-grained understanding of how movement-specific information is routed via molecularly distinct projection pathways.

We also found that PT and IT neurons displaying high decoding accuracy were distributed across FOVs. This lack of functional clustering differs from the proposed modular organization of directionally tuned cells in primate motor cortex, where neurons with a similar preferred direction tend to cluster into vertically oriented minicolumns approximately 50–100 μm wide, repeated every 250 μm (Amirikian and Georgopoulos, 2003; Cheney et al., 1985; Georgopoulos et al., 2007; Jones and Wise, 1977), but consistent with the distributed spatial organization of direction-specific layer 5B projection neurons in mouse anterolateral motor cortex during execution of a whisker-based object location discrimination task (Li et al., 2015). The apparent lack of spatial clustering in CFA is unlikely to be due to reduced sensitivity of our analysis methods because 95% confidence intervals provide a lower bound indication of cluster size so that spatial clusters based on decoding accuracy would have to be less than ~50 μm. Similarly, we found no evidence of temporal clustering in neurons with high (movement-specific) or low (movement-invariant) decoding accuracy, as expected, given that the onset of PT and IT neuron activity changes occurred ~300 ms prior to movement and tiled the peri-movement period. Our work extends previous findings in superficial layers of motor cortex showing that neurons with task-related response properties are spatially intermingled (Galiñanes et al., 2018; Huber et al., 2012), supporting a model where movement-specific signaling in layer 5B is distributed across small but distinct subpopulations of projection neurons. The flexible routing of information through distributed descending projection pathways could, in principle, provide a mechanism for differentially controlling movement variables necessary for executing a wide repertoire of limb movements.

Limitations of the study

In the present study, we suggest that layer 5B population dynamics largely reflect movement-invariant signaling, whereas relatively small subpopulations of projection neurons convey movement-specific information. However, our task design was limited to two diametrically opposing movements along a single axis, where the starting posture for push and pull movements differed. A fuller understanding of how movement-specific signaling is organized across mouse layer 5 projection neurons would require implementation of a task that incorporates multiple movement trajectories initiated from the same start position (e.g., a center-out multi-direction joystick or reaching task) or a task in which mice learn to perform multiple distinct actions (e.g., lever push and reach to grab). Another limitation of our study is that we only sampled the activity of identified projection neurons in upper layer 5B. Given the known depth dependence of top-down and long-range inputs in layer 5 (Anderson et al., 2010; Weiler et al., 2008; Hooks et al., 2013) and laminar organization of output neurons based on projection targets (Economo et al., 2018), encoding of movement specificity is likely to differ depending on cortical depth. This could be addressed using methods to image deeper within the cortex (e.g., using a glass prism or 3-photon microscopy) or high-density silicone probe recordings with optogenetic identification of projection neuron class.

STAR★METHODS

Detailed methods are provided in the online version of this paper and include the following:

- KEY RESOURCES TABLE
- RESOURCE AVAILABILITY
  - Lead contact
  - Materials availability
  - Data and code availability
- EXPERIMENTAL MODEL AND SUBJECT DETAILS
- METHOD DETAILS
  - General surgery
  - Behavioral training
  - Forelimb kinematic tracking
  - *In vivo* pharmacology
  - Quantifying muscimol diffusion
  - Retrograde tracing
  - Immunohistochemistry
  - 2-photon imaging
  - Trial-to-trial correlations

- Extracellular recording and spike sorting
- Neural decoding
- Dimensionality reduction
- Spatiotemporal mapping

- QUANTIFICATION AND STATISTICAL ANALYSIS

SUPPLEMENTAL INFORMATION

Supplemental information can be found online at https://doi.org/10.1016/j.celrep.2022.110801.

ACKNOWLEDGMENTS

We are grateful to Gülsen Sürmeli, Matt Nolan, and members of the Nolan, Duguid, and Sürmeli labs for experimental discussions and comments on the manuscript; Nick Steinmetz for the suggested design of the author contribution matrix; and Tiago Branco and Kostas Betsios for Mantis64. AAV-GCaMP6s was a gift from Douglas Kim and the GENIE Project (Addgene 100844-AAV1). AAV-pgk-Cre was a gift from Patrick Aebischer (Addgene viral prep 24593-AAVrg). pAAV-CAG-Flex-mRuby2-GSG-P2A-GCaMP6s-WPRE-pA was a gift from Tobias Bonhoeffer, Mark Huebener, and Tobias Rose (Addgene viral prep 68717-AAV1). Confocal microscopy was performed in the IMPACT Imaging Facility at the University of Edinburgh. Research was supported by grants from the Biotechnology and Biological Sciences Research Council (BB/R018537/1 to I.D.), the DFG fellowship program (AM 443/1-1 to J.J.A.), the Shirley Foundation, a Simons Initiative for the Developing Brain (SIDB) PhD studentship (to C.E.), an A*STAR PhD studentship (to B.P.), and a Wellcome Senior Research Fellowship (110131/Z/15/Z to I.D.).

AUTHOR CONTRIBUTIONS

Conceptualization, B.P., J.J.A., and I.D.; methodology & investigation, S.P.C., J.J.A., B.P., J.D., Y.W., C.E., M.C., T.C., L.M., M.H.H., and I.D.; resources, J.J.A., Y.W., M.C., A.A.F., and M.H.H.; review & editing, all authors.

DECLARATION OF INTEREST

The authors declare no competing interests.

Received: November 20, 2020
Revised: November 15, 2021
Accepted: April 18, 2022
Published: May 10, 2022

REFERENCES

Amirikian, B., and Georgopoulos, A.P. (2003). Modular organization of directionally tuned cells in the motor cortex: is there a short-range order? Proc. Natl. Acad. Sci. U S A *100*, 12474–12479. https://doi.org/10.1073/pnas.2037719100.

Anderson, C.T., Sheets, P.L., Kiritani, T., and Shepherd, G.M.G. (2010). Sublayer-specific microcircuits of corticospinal and corticostriatal neurons in motor cortex. Nat. Neurosci. *13*, 739–744. https://doi.org/10.1038/nn.2538.

Baker, A., Kalmbach, B., Morishima, M., Kim, J., Juavinett, A., Li, N., and Dembrow, N. (2018). Specialized subpopulations of deep-layer pyramidal neurons in the neocortex: bridging cellular properties to functional consequences. J. Neurosci. *38*, 5441–5455. https://doi.org/10.1523/jneurosci.0150-18.2018.

Bartlett, M.S., and Fowler, R.H. (1937). Properties of sufficiency and statistical tests. Proc. R. Soc. Lond. Ser. A Math. Phys. Sci. *160*, 268–282.

Brown, S.P., and Hestrin, S. (2009). Intracortical circuits of pyramidal neurons reflect their long-range axonal targets. Nature *457*, 1133–1136. https://doi.org/10.1038/nature07658.

Chen, T.-W., Li, N., Daie, K., and Svoboda, K. (2017). A map of anticipatory activity in mouse motor cortex. Neuron *94*, 866–879.e4. https://doi.org/10.1016/j.neuron.2017.05.005.

Cheney, P.D., Fetz, E.E., and Palmer, S.S. (1985). Patterns of facilitation and suppression of antagonist forelimb muscles from motor cortex sites in the awake monkey. J. Neurophysiol. *53*, 805–820. https://doi.org/10.1152/jn.1985.53.3.805.

Churchland, M.M., Cunningham, J.P., Kaufman, M.T., Foster, J.D., Nuyujukian, P., Ryu, S.I., and Shenoy, K.V. (2012). Neural population dynamics during reaching. Nature *487*, 51–56. https://doi.org/10.1038/nature11129.

Churchland, M.M., Cunningham, J.P., Kaufman, M.T., Ryu, S.I., and Shenoy, K.V. (2010). Cortical preparatory activity: representation of movement or first cog in a dynamical machine? Neuron *68*, 387–400. https://doi.org/10.1016/j.neuron.2010.09.015.

Cunningham, J.P., and Yu, B.M. (2014). Dimensionality reduction for large-scale neural recordings. Nat. Neurosci. *17*, 1500–1509. https://doi.org/10.1038/nn.3776.

Dacre, J., Colligan, M., Clarke, T., Ammer, J.J., Schiemann, J., Chamosa-Pino, V., Claudi, F., Harston, J.A., Eleftheriou, C., Pakan, J.M.P., et al. (2021). A cerebellar-thalamocortical pathway drives behavioral context-dependent movement initiation. Neuron *109*, 2326–2338. https://doi.org/10.1016/j.neuron.2021.05.016.

Economo, M.N., Viswanathan, S., Tasic, B., Bas, E., Winnubst, J., Menon, V., Graybuck, L.T., Nguyen, T.N., Smith, K.A., Yao, Z., et al. (2018). Distinct descending motor cortex pathways and their roles in movement. Nature *563*, 79–84. https://doi.org/10.1038/s41586-018-0642-9.

Elsayed, G.F., Lara, A.H., Kaufman, M.T., Churchland, M.M., and Cunningham, J.P. (2016). Reorganization between preparatory and movement population responses in motor cortex. Nat. Commun. *7*, 13239. https://doi.org/10.1038/ncomms13239.

Estebanez, L., Hoffmann, D., Voigt, B.C., and Poulet, J.F.A. (2017). Parvalbumin-expressing GABAergic neurons in primary motor cortex signal reaching. Cell Rep. *20*, 308–318. https://doi.org/10.1016/j.celrep.2017.06.044.

Evarts, E.V. (1968). Relation of pyramidal tract activity to force exerted during voluntary movement. J. Neurophysiol. *31*, 14–27. https://doi.org/10.1152/jn.1968.31.1.14.

Galiñanes, G.L., Bonardi, C., and Huber, D. (2018). Directional reaching for water as a cortex-dependent behavioral framework for mice. Cell Rep. *22*, 2767–2783. https://doi.org/10.1016/j.celrep.2018.02.042.

Georgopoulos, A.P., Kalaska, J.F., Caminiti, R., and Massey, J.T. (1982). On the relations between the direction of two-dimensional arm movements and cell discharge in primate motor cortex. J. Neurosci. *2*, 1527–1537. https://doi.org/10.1523/jneurosci.02-11-01527.1982.

Georgopoulos, A.P., Merchant, H., Naselaris, T., and Amirikian, B. (2007). Mapping of the preferred direction in the motor cortex. Proc. Natl. Acad. Sci. U S A *104*, 11068–11072. https://doi.org/10.1073/pnas.0611597104.

Guo, J.-Z., Graves, A.R., Guo, W.W., Zheng, J., Lee, A., Rodríguez-González, J., Li, N., Macklin, J.J., Phillips, J.W., Mensh, B.D., et al. (2015). Cortex commands the performance of skilled movement. Elife *4*, e10774. https://doi.org/10.7554/elife.10774.

Hocherman, S., and Wise, S.P. (1991). Effects of hand movement path on motor cortical activity in awake, behaving rhesus monkeys. Exp. Brain Res. *83*, 285–302. https://doi.org/10.1007/bf00231153.

Hooks, B.M., Mao, T., Gutnisky, D.A., Yamawaki, N., Svoboda, K., and Shepherd, G.M.G. (2013). Organization of cortical and thalamic input to pyramidal neurons in mouse motor cortex. J. Neurosci. *33*, 748–760. https://doi.org/10.1523/jneurosci.4338-12.2013.

Hooks, B.M., Papale, A.E., Paletzki, R.F., Feroze, M.W., Eastwood, B.S., Couey, J.J., Winnubst, J., Chandrashekar, J., and Gerfen, C.R. (2018). Topographic precision in sensory and motor corticostriatal projections varies across cell type and cortical area. Nat. Commun. *9*, 3549. https://doi.org/10.1038/s41467-018-05780-7.

Huber, D., Gutnisky, D.A., Peron, S., O'Connor, D.H., Wiegert, J.S., Tian, L., Oertner, T.G., Looger, L.L., and Svoboda, K. (2012). Multiple dynamic representations in the motor cortex during sensorimotor learning. Nature *484*, 473–478. https://doi.org/10.1038/nature11039.

Hwang, E.J., Dahlen, J.E., Hu, Y.Y., Aguilar, K., Yu, B., Mukundan, M., Mitani, A., and Komiyama, T. (2019). Disengagement of motor cortex from movement control during long-term learning. Sci. Adv. *5*, eaay0001. https://doi.org/10.1126/sciadv.aay0001.

Hwang, E.J., Dahlen, J.E., Mukundan, M., and Komiyama, T. (2021). Disengagement of motor cortex during long-term learning tracks the performance level of learned movements. J. Neurosci. *41*, 7029–7047. https://doi.org/10.1523/jneurosci.3049-20.2021.

Isomura, Y., Harukuni, R., Takekawa, T., Aizawa, H., and Fukai, T. (2009). Microcircuitry coordination of cortical motor information in self-initiation of voluntary movements. Nat. Neurosci. *12*, 1586–1593. https://doi.org/10.1038/nn.2431.

Jones, E.G., and Wise, S.P. (1977). Size, laminar and columnar distribution of efferent cells in the sensory-motor cortex of monkeys. J. Comp. Neurol. *175*, 391–437. https://doi.org/10.1002/cne.901750403.

Jun, J.J., Steinmetz, N.A., Siegle, J.H., Denman, D.J., Bauza, M., Barbarits, B., Lee, A.K., Anastassiou, C.A., Andrei, A., Aydın, Ç., et al. (2017). Fully integrated silicon probes for high-density recording of neural activity. Nature *551*, 232–236. https://doi.org/10.1038/nature24636.

Kaifosh, P., Zaremba, J.D., Danielson, N.B., and Losonczy, A. (2014). SIMA: Python software for analysis of dynamic fluorescence imaging data. Front. Neuroinform. *8*, 80. https://doi.org/10.3389/fninf.2014.00080.

Kaufman, M.T., Churchland, M.M., Ryu, S.I., and Shenoy, K.V. (2014). Cortical activity in the null space: permitting preparation without movement. Nat. Neurosci. *17*, 440–448. https://doi.org/10.1038/nn.3643.

Kaufman, M.T., Seely, J.S., Sussillo, D., Ryu, S.I., Shenoy, K.V., and Churchland, M.M. (2016). The largest response component in the motor cortex reflects movement timing but not movement type. eNeuro *3*, ENEURO.0085-16.2016. https://doi.org/10.1523/eneuro.0085-16.2016.

Kawai, R., Markman, T., Poddar, R., Ko, R., Fantana, A.L., Dhawale, A.K., Kampff, A.R., and Ölveczky, B.P. (2015). Motor cortex is required for learning but not for executing a motor skill. Neuron *86*, 800–812. https://doi.org/10.1016/j.neuron.2015.03.024.

Keemink, S.W., Lowe, S.C., Pakan, J.M.P., Dylda, E., van Rossum, M.C.W., and Rochefort, N.L. (2018). FISSA: a neuropil decontamination toolbox for calcium imaging signals. Sci. Rep. *8*, 3493. https://doi.org/10.1038/s41598-018-21640-2.

Kiritani, T., Wickersham, I.R., Sebastian Seung, H., and Shepherd, G.M.G. (2012). Hierarchical connectivity and connection-specific dynamics in the corticospinal–corticostriatal microcircuit in mouse motor cortex. J. Neurosci. *32*, 4992–5001. https://doi.org/10.1523/jneurosci.4759-11.2012.

Kita, T., and Kita, H. (2012). The subthalamic nucleus is one of multiple innervation sites for long-range corticofugal axons: a single-axon tracing study in the rat. J. Neurosci. *32*, 5990–5999. https://doi.org/10.1523/jneurosci.5717-11.2012.

Kurtzer, I., Herter, T.M., and Scott, S.H. (2005). Random change in cortical load representation suggests distinct control of posture and movement. Nat. Neurosci. *8*, 498–504. https://doi.org/10.1038/nn1420.

Lawrence, D.G., and Kuypers, H.G. (1968). The functional organization of the motor system in the monkey. I. The effects of bilateral pyramidal lesions. Brain *91*, 1–14. https://doi.org/10.1093/brain/91.1.1.

Lemon, R.N. (2008). Descending pathways in motor control. Annu. Rev. Neurosci. *31*, 195–218. https://doi.org/10.1146/annurev.neuro.31.060407.125547.

Levesque, M., Charara, A., Gagnon, S., Parent, A., and Deschenes, M. (1996). Corticostriatal projections from layer V cells in rat are collaterals of long-range corticofugal axons. Brain Res. *709*, 311–315. https://doi.org/10.1016/0006-8993(95)01333-4.

Levy, S., Lavzin, M., Benisty, H., Ghanayim, A., Dubin, U., Achvat, S., Brosh, Z., Aeed, F., Mensh, B.D., Schiller, Y., et al. (2020). Cell-type-specific outcome representation in the primary motor cortex. Neuron *107*, 954–971.e9. https://doi.org/10.1016/j.neuron.2020.06.006.

Li, N., Chen, T.-W., Guo, Z.V., Gerfen, C.R., and Svoboda, K. (2015). A motor cortex circuit for motor planning and movement. Nature *519*, 51–56. https://doi.org/10.1038/nature14178.

Martin, J.H., and Ghez, C. (1991). Impairments in reaching during reversible inactivation of the distal forelimb representation of the motor cortex in the cat. Neurosci. Lett. *133*, 61–64. https://doi.org/10.1016/0304-3940(91)90057-z.

Maruoka, H., Nakagawa, N., Tsuruno, S., Sakai, S., Yoneda, T., and Hosoya, T. (2017). Lattice system of functionally distinct cell types in the neocortex. Science *358*, 610–615. https://doi.org/10.1126/science.aam6125.

Mathis, A., Mamidanna, P., Cury, K.M., Abe, T., Murthy, V.N., Mathis, M.W., and Bethge, M. (2018). DeepLabCut: markerless pose estimation of user-defined body parts with deep learning. Nat. Neurosci. *21*, 1281–1289. https://doi.org/10.1038/s41593-018-0209-y.

Messier, J., and Kalaska, J.F. (2000). Covariation of primate dorsal premotor cell activity with direction and amplitude during a memorized-delay reaching task. J. Neurophysiol. *84*, 152–165. https://doi.org/10.1152/jn.2000.84.1.152.

Miri, A., Warriner, C.L., Seely, J.S., Elsayed, G.F., Cunningham, J.P., Churchland, M.M., and Jessell, T.M. (2017). Behaviorally selective engagement of short-latency effector pathways by motor cortex. Neuron *95*, 683–696.e11. https://doi.org/10.1016/j.neuron.2017.06.042.

Molyneaux, B.J., Arlotta, P., Menezes, J.R.L., and Macklis, J.D. (2007). Neuronal subtype specification in the cerebral cortex. Nat. Rev. Neurosci. *8*, 427–437. https://doi.org/10.1038/nrn2151.

Moran, D.W., and Schwartz, A.B. (1999). Motor cortical representation of speed and direction during reaching. J. Neurophysiol. *82*, 2676–2692. https://doi.org/10.1152/jn.1999.82.5.2676.

Morishima, M., and Kawaguchi, Y. (2006). Recurrent connection patterns of corticostriatal pyramidal cells in frontal cortex. J. Neurosci. *26*, 4394–4405. https://doi.org/10.1523/jneurosci.0252-06.2006.

Morishima, M., Morita, K., Kubota, Y., and Kawaguchi, Y. (2011). Highly differentiated projection-specific cortical subnetworks. J. Neurosci. *31*, 10380–10391. https://doi.org/10.1523/jneurosci.0772-11.2011.

Muñoz-Castañeda, R., Zingg, B., Matho, K.S., Chen, X., Wang, Q., Foster, N.N., Li, A., Narasimhan, A., Hirokawa, K.E., Huo, B., et al. (2021). Cellular anatomy of the mouse primary motor cortex. Nature *598*, 159–166. https://doi.org/10.1038/s41586-021-03970-w.

Nelson, A., Abdelmesih, B., and Costa, R.M. (2021). Corticospinal populations broadcast complex motor signals to coordinated spinal and striatal circuits. Nat. Neurosci. *24*, 1721–1732. https://doi.org/10.1038/s41593-021-00939-w.

Oswald, M.J., Tantirigama, M.L.S., Sonntag, I., Hughes, S.M., and Empson, R.M. (2013). Diversity of layer 5 projection neurons in the mouse motor cortex. Front. Cell Neurosci. *7*, 174. https://doi.org/10.3389/fncel.2013.00174.

Pachitariu, M., Steinmetz, N., Kadir, S., and Carandini, M. (2016). Kilosort: real-time spike-sorting for extracellular electrophysiology with hundreds of channels. Preprint at bioRxiv. https://doi.org/10.1101/061481.

Panigrahi, B., Martin, K.A., Li, Y., Graves, A.R., Vollmer, A., Olson, L., Mensh, B.D., Karpova, A.Y., and Dudman, J.T. (2015). Dopamine is required for the neural representation and control of movement vigor. Cell *162*, 1418–1430. https://doi.org/10.1016/j.cell.2015.08.014.

Paninski, L., Fellows, M.R., Hatsopoulos, N.G., and Donoghue, J.P. (2004). Spatiotemporal tuning of motor cortical neurons for hand position and velocity. J. Neurophysiol. *91*, 515–532. https://doi.org/10.1152/jn.00587.2002.

Park, J., Phillips, J.W., Guo, J.Z., Martin, K.A., Hantman, A.W., and Dudman, J.T. (2022). Motor cortical output for skilled forelimb movement is selectively distributed across projection neuron classes. Sci. Adv. *8*, 1–11. https://doi.org/10.1126/sciadv.abj5167.

Paxinos, G., and Franklin, K. (2008). The mouse brain in stereotaxic coordinates. In Compact: The Coronal Plates and Diagrams, 3rd edition (Elsevier Science Publishing/Academic Press).

Peters, A.J., Lee, J., Hedrick, N.G., O'Neil, K., and Komiyama, T. (2017). Reorganization of corticospinal output during motor learning. Nat. Neurosci. *20*, 1133–1141. https://doi.org/10.1038/nn.4596.

Podgorski, K., and Ranganathan, G. (2016). Brain heating induced by near-infrared lasers during multiphoton microscopy. J. Neurophysiol. *116*, 1012–1023. https://doi.org/10.1152/jn.00275.2016.

Reiner, A., Hart, N.M., Lei, W., and Deng, Y. (2010). Corticostriatal projection neurons - dichotomous types and dichotomous functions. Front. Neuroanat. *4*, 142. https://doi.org/10.3389/fnana.2010.00142.

Riehle, A., Kornblum, S., and Requin, J. (1994). Neuronal coding of stimulus-response association rules in the motor cortex. Neuroreport *5*, 2462–2464. https://doi.org/10.1097/00001756-199412000-00014.

Ruder, L., and Arber, S. (2019). Brainstem circuits controlling action diversification. Annu. Rev. Neurosci. *42*, 485–504. https://doi.org/10.1146/annurev-neuro-070918-050201.

Rueden, C.T., Schindelin, J., Hiner, M.C., DeZonia, B.E., Walter, A.E., Arena, E.T., and Eliceiri, K.W. (2017). ImageJ2: ImageJ for the next generation of scientific image data. BMC Bioinf. *18*, 529. https://doi.org/10.1186/s12859-017-1934-z.

Sauerbrei, B.A., Guo, J.-Z., Cohen, J.D., Mischiati, M., Guo, W., Kabra, M., Verma, N., Mensh, B., Branson, K., and Hantman, A.W. (2019). Cortical pattern generation during dexterous movement is input-driven. Nature *577*, 386–391. https://doi.org/10.1038/s41586-019-1869-9.

Schiemann, J., Puggioni, P., Dacre, J., Pelko, M., Domanski, A., van Rossum, M.C.W., and Duguid, I. (2015). Cellular mechanisms underlying behavioral state-dependent bidirectional modulation of motor cortex output. Cell Rep. *11*, 1319–1330. https://doi.org/10.1016/j.celrep.2015.04.042.

Schindelin, J., Arganda-Carreras, I., Frise, E., Kaynig, V., Longair, M., Pietzsch, T., Preibisch, S., Rueden, C., Saalfeld, S., Schmid, B., et al. (2012). Fiji: an open-source platform for biological-image analysis. Nat. Methods *9*, 676–682. https://doi.org/10.1038/nmeth.2019.

Seabold, S., and Perktold, J. (2010). Statsmodels: econometric and statistical modeling with python. Paper presented at: Proceedings of the 9th Python in Science Conference (Austin, TX).

Shepherd, G.M.G. (2013). Corticostriatal connectivity and its role in disease. Nat. Rev. Neurosci. *14*, 278–291. https://doi.org/10.1038/nrn3469.

Soma, S., Saiki, A., Yoshida, J., Ríos, A., Kawabata, M., Sakai, Y., and Isomura, Y. (2017). Distinct laterality in forelimb-movement representations of rat primary and secondary motor cortical neurons with intratelencephalic and pyramidal tract projections. J. Neurosci. *37*, 10904–10916. https://doi.org/10.1523/jneurosci.1188-17.2017.

Stopfer, M., Jayaraman, V., and Laurent, G. (2003). Intensity versus identity coding in an olfactory system. Neuron *39*, 991–1004. https://doi.org/10.1016/j.neuron.2003.08.011.

Sussillo, D., Churchland, M.M., Kaufman, M.T., and Shenoy, K.V. (2015). A neural network that finds a naturalistic solution for the production of muscle activity. Nat. Neurosci. *18*, 1025–1033. https://doi.org/10.1038/nn.4042.

Thach, W.T. (1978). Correlation of neural discharge with pattern and force of muscular activity, joint position, and direction of intended next movement in motor cortex and cerebellum. J. Neurophysiol. *41*, 654–676. https://doi.org/10.1152/jn.1978.41.3.654.

Ueta, Y., Otsuka, T., Morishima, M., Ushimaru, M., and Kawaguchi, Y. (2014). Multiple layer 5 pyramidal cell subtypes relay cortical feedback from secondary to primary motor areas in rats. Cereb. Cortex *24*, 2362–2376. https://doi.org/10.1093/cercor/bht088.

Wang, X., Liu, Y., Li, X., Zhang, Z., Yang, H., Zhang, Y., Williams, P.R., Alwahab, N.S.A., Kapur, K., Yu, B., et al. (2017). Deconstruction of corticospinal circuits for goal-directed motor skills. Cell *171*, 440–455.e14. https://doi.org/10.1016/j.cell.2017.08.014.

Wei, Z., Lin, B.-J., Chen, T.-W., Daie, K., Svoboda, K., and Druckmann, S. (2020). A comparison of neuronal population dynamics measured with calcium imaging and electrophysiology. PLoS Comput. Biol. *16*, e1008198. https://doi.org/10.1371/journal.pcbi.1008198.

Weiler, N., Wood, L., Yu, J., Solla, S.A., and Shepherd, G.M.G. (2008). Top-down laminar organization of the excitatory network in motor cortex. Nat. Neurosci. *11*, 360–366. https://doi.org/10.1038/nn2049.

Weinrich, M., Wise, S.P., and Mauritz, K.H. (1984). A neurophysiological study of the premotor cortex in the rhesus monkey. Brain *107*, 385–414. https://doi.org/10.1093/brain/107.2.385.

Wilson, C.J. (1987). Morphology and synaptic connections of crossed corticostriatal neurons in the rat. J. Comp. Neurol. *263*, 567–580. https://doi.org/10.1002/cne.902630408.

Winnubst, J., Bas, E., Ferreira, T.A., Wu, Z., Economo, M.N., Edson, P., Arthur, B.J., Bruns, C., Rokicki, K., Schauder, D., et al. (2019). Reconstruction of 1,000 projection neurons reveals new cell types and organization of long-range connectivity in the mouse brain. Cell *179*, 268–281.e13. https://doi.org/10.1016/j.cell.2019.07.042.

Yttri, E.A., and Dudman, J.T. (2016). Opponent and bidirectional control of movement velocity in the basal ganglia. Nature *533*, 402–406. https://doi.org/10.1038/nature17639.

Zhou, Z., and Tin, C. (2021). Effective and efficient neural networks for spike inference from *in vivo* calcium imaging. Preprint at bioRxiv. https://doi.org/10.1101/2021.08.30.458217.

Zong, W., Heldt, T., Moody, G.B., and Mark, R.G. (2003). An open-source algorithm to detect onset of arterial blood pressure pulses. In Computers in Cardiology, 2003 (IEEE), pp. 259–262. ieeexplore.ieee.org.

STAR★METHODS

KEY RESOURCES TABLE

REAGENT or RESOURCE	SOURCE	IDENTIFIER
Antibodies		
AlexaFluor-568 goat anti-mouse	Invitrogen	CAT#: A-21124; AB_2535766
Anti-NeuN Antibody, clone A60	Sigma Aldrich	Cat#: MAB377
Bacterial and virus strains		
AAV1-Syn-GCaMP6s	Penn Vector Core	#100844-AAV1
AAV-pkg-Cre	Addgene	#24593-AAVrg
pAAV-CAG-Flex-mRuby2-GSG-P2A-GCaMP6s-WPREpA	Addgene	#68717-AAV1
Chemicals, peptides, and recombinant proteins		
Muscimol hydrobromide	Sigma-Aldrich, Missouri, USA	Cat#: G019-5MG
Muscimol, BODIPY TMR-X Conjugate	Thermo Fisher Scientific	Cat#: M23400
Red Retrobeads™	Lumaflor	N/A
Green Retrobeads™	Lumaflor	N/A
Fast Blue	Polysciences	Cat#: 17740
Vybrant DiI Cell-Labeling	Thermo Fisher Scientific	Cat#: V22885
Experimental models: Organisms/strains		
Mouse: C57BL/6J	The Jackson Laboratory	RRID: IMSR_JAX:000664
Software and algorithms		
MATLAB	MathWorks (https://www.mathworks.com/)	RRID: SCR_001622
Python 3	Python (https://www.python.org/)	RRID: SCR_008394
Streampix 7.0	Norpix (https://www.norpix.com/products/streampix/streampix.php)	RRID:SCR_015773
SpikeGLX	(http://billkarsh.github.io/SpikeGLX/)	N/A
Mantis64	https://www.mantis64.com/	N/A
Kilosort3	https://github.com/MouseLand/Kilosort	N/A
Phy	Jun et al., 2017 (https://github.com/cortex-lab/phy)	N/A
FIJI	Schindelin et al., 2012 (https://github.com/fiji)	RRID:SCR_002285
Deeplabcut	Adaptive Motor Control Lab (https://github.com/DeepLabCut/DeepLabCut)	N/A
FISSA	Keemink et al., 2018	N/A
SIMA 1.3.2	Kaifosh et al., 2014	
Onset detection algorithm	Zong et al., 2003	N/A
Arduino IDE 1.6.5	Arduino (https://www.arduino.cc/en/software)	N/A
NIS-Elements	Nikon (https://www.microscope.healthcare.nikon.com/products/software)	RRID:SCR_014329
LotosScan	LabVIEW version 8.2; National Instruments	N/A

(*Continued on next page*)

Continued

REAGENT or RESOURCE	SOURCE	IDENTIFIER
SciScan	Scientifica (https://www.scientifica.uk.com/products/scientifica-sciscan)	N/A
Other		
Neuropixels probes	IMEC	Neuropixels 1.0
Laser, Ti:Sapphire pulsed	Coherent	Chameleon Vision-S
Arduino UNO	Arduino (https://www.arduino.cc/en/Guide/ArduinoUno/)	RRID:SCR_017284

RESOURCE AVAILABILITY

Lead contact

Further information and requests for resources and reagents should be directed to and will be fulfilled by the Lead Contact, Ian Duguid (ian.duguid@ed.ac.uk).

Materials availability

This study did not generate new unique reagents.

Data and code availability

Data reported in this paper will be shared by the lead contact upon request. All original code has been deposited at https://github.com/DuguidLab and is publicly available as of the date of publication. Any additional information required to reanalyze the data reported in this paper is available from the lead contact upon request.

EXPERIMENTAL MODEL AND SUBJECT DETAILS

Male adult C57BL/6J wild-type mice (5-12 weeks old, 20-30 g, 1-4 animals per cage) were maintained on a reversed 12:12 hour light:-dark cycle and provided *ad libitum* access to food and water as well as environmental enrichment (e.g., cardboard tubes, plastic domes, chewing sticks, and rope ladders). All experiments and procedures were approved by the University of Edinburgh local ethical review committee and performed under license from the UK Home Office in accordance with the Animal (Scientific Procedures) Act 1986.

METHOD DETAILS

General surgery

Surgical procedures were performed under ~1.5% isoflurane anaesthesia and each animal received fluid replacement therapy (0.5 ml sterile Ringer's solution), buprenorphine (0.05 mg/kg) and either carprofen (4 mg/kg) or dexamethasone (2 mg/kg) for pain relief and to reduce inflammation. At 24 and 48 hours, carprofen (4 mg/kg) was administered for post-operative pain relief. Craniotomies were performed in a stereotactic frame (David Kopf Instruments, CA, USA) using a hand-held dentist drill with 0.5 mm burr. A small lightweight headplate (0.5 g) was implanted on the surface of the skull using cyanoacrylate glue and dental cement (Lang Dental, IL, USA) and mice were left for at least 48 hours to recover.

Behavioral training

After recovery from head plate surgery, mice were handled extensively before being head restrained and habituated to a custom forelimb lever push / pull behavioral setup. Mice were trained to perform two diametrically opposing movements (4 mm push or pull) in response to a 6 kHz auditory cue to obtain a 5 μl water reward. Mice rested their right forepaw on a stationary lever while making push or pull movements with their left forepaw. Upon completion of a successful push or pull (determined by the status of IR beams at either end of the lever travel), the moveable lever was locked in place for the duration of the reward period (3 s) and the water reward was delivered by an automated spout - both locking mechanism and spout were controlled by micro servo motors (HXT900, HexTronik). To increase task engagement, mice were placed on a water control paradigm (1 ml/day) and weighed daily to ensure body weight remained above 85% of baseline. Mice were trained once per day for 30 mins and advanced through different phases of the task once they achieved > 50 rewards in two consecutive sessions or > 70 rewards in a single session. Initially, mice were required to perform uncued push and pull movements to obtain rewards (phase 1). Next, an auditory cue was introduced with pseudo-random inter-trial-interval (ITI) of 4-6 s and a response window of 10 s (phase 2). During the ITI, mice had to hold the move-

able lever still as spontaneous movements of the lever within the ITI triggered a reset and the lever was locked in the original position for 1 s. The response window was gradually reduced to 5 (phase 3) and then 2 s (phase 4) across training sessions. Mice were deemed "expert" after achieving > 70 rewards on two consecutive days of training with a response window of 2 s. During 2-photon imaging experiments (see below), a 1 s delay between completion of a successful movement and reward delivery was introduced to temporally separate movement- and reward-related activity.

Forelimb kinematic tracking

Behavior was recorded using a high-speed camera (60 fps Prosilica GC780C, Allied Vision, Germany or 100 - 300 fps Mako U U-029, Allied Vision - cell-type specific calcium imaging and *in vivo* pharmacology) and acquired using Streampix 7 (Norpix, Canada) or Mantis64 (https://www.mantis64.com/). To measure gross forelimb movement, a region of interest (ROI) was manually drawn around the left forelimb and the frame-to-frame difference in pixel intensity was calculated using the formula: $MI_f = \sum_{i=1}^{N}(c_{f+1,i} - c_{f,i})^2$, where $c_{f,i}$ is the grayscale level of pixel i in frame f. The resulting motion index was smoothed with a 1 s LOESS filter then aligned to behaviorally relevant time points (lever displacement, cue presentation etc.), with videos and behavior resampled to a common sampling rate. Motion index onsets were calculated by aligning the motion index to the lever movement and identifying the first point prior to movement where mean motion index was > threshold (mean upper bound of 95% confidence interval during baseline). Directional tracking of the forelimb and lever movement was performed using Deep Lab Cut (Mathis et al., 2018). Tracking data were aligned to cue presentation, baselined to mean xy position during the 100 ms prior to cue and then cropped between movement initiation and movement completion. For presentation, trials of different durations were resampled to a fixed length to enable a mean trajectory to be plotted across multiple trials.

In vivo pharmacology

To assess the behavioral effects of caudal forelimb area (CFA; N = 10) or hind limb motor cortex ($M1_{hl}$; N = 5) inactivation, 'expert' mice had a small burr hole drilled directly above the target area (CFA: 1.6 mm lateral, 0.6 mm rostral to bregma; $M1_{hl}$: 1.25 mm lateral, 1.25 caudal to bregma) before being left to recover for > 90 mins. After 10 mins of baseline behavior, the lever was locked and a small volume of the $GABA_A$ receptor agonist muscimol (200 nl, 2 mM) dissolved in external saline solution (containing 150 mM NaCl, 2.5 mM KCl, 10 mM HEPES, 1.5 mM $CaCl_2$ and 1 mM $MgCl_2$, adjusted to pH 7.3) was injected into the target area. Each injection site was at a depth of 0.7 mm below the cortical surface. To confirm the anatomical location of drug injection, 1% w/v of retrobeads (red, Lumaflor Inc.) was included in the injected solution. A subset of mice (N = 5/10) also had saline injected into CFA (vehicle only; injection was perfromed on a different day). In these experiments, mice were randomly assigned to drug or control groups (each mouse received one injection of muscimol and one injection of saline) and experiments were blinded. After each experiment, mice were transcardially perfused and coronal (60 μm) or sagittal (100 μm) sections were cut with a vibratome (Leica VT1000S), mounted with Vectashield mounting medium (H-1000, Vector Laboratories), imaged using a fluorescence microscope (Leica DMR, 5x objective) and manually referenced to the Paxinos and Franklin Mouse Brain Atlas (Paxinos and Franklin, 2008). Behavioral metrics were analyzed by comparing videos of 10 mins pre and post injection. Behavioral video data for all pharmacology experiments was captured using a high-speed camera (Mako U U-029, Allied Vision), and paw position accuracy was calculated as the proportion of trials in which mice were holding the moveable lever at time of cue presentation.

Quantifying muscimol diffusion

To measure muscimol diffusion, a small volume of muscimol-BODIPY TMR-X Conjugate (ThermoFisher Scientific; dissolved in 0.1 PBS w/1% dimethyl sulfoxide) was injected into CFA (200 nl of 2 mM at 4 sites centered on 1.6 mm lateral, 0.6 mm rostral to bregma at a depth of 0.7 mm below the cortical surface). To mark the center of the injection site, pipettes were backfilled with a small volume (~20 nl) of green retrobeads (Lumafluor Inc.) prior to filling with muscimol-BODIPY. Following injection, animals were transcardially perfused and brains snap-frozen on dry ice 10 minutes after completion of the muscimol injection. Brains were stored on dry ice, coronal sections (60 μm) collected with a cryostat (Leica) at -20°C and imaged with a light microscope (Leica DMR, 5x objective). We assumed maximum fluorescence ≈ maximum injected concentration and that grayscale pixel intensity was proportional to muscimol-BODIPY concentration. Therefore, pixel values were thresholded at the equivalent pixel value of an EC_{20} concentration of muscimol and fluorescence outlines were drawn to generate a 'spread profile'. Green retrobeads were used to mark the center of each injection, and images were aligned to the injection center of gravity. From the aligned profiles, a modal spread profile (i.e., pixels with positive grayscale values across all mice) was generated and aligned to the Paxinos and Franklin Mouse Brain Atlas (Paxinos and Franklin, 2008).

Retrograde tracing

To selectively label pyramidal tract (PT) neurons in layer 5B of CFA, red retrobeads (Lumafluor, USA) were injected into the pons (4.0 mm caudal and 0.4 mm lateral to bregma ipsilateral to the target CFA), delivered via pulled glass pipettes (5μl, Drummond Scientific, PA, USA; 10–20 nl/min) using an automated injection system (Model Picospritzer iii, Parker, NH, USA). Injections were made at 4 sites (100 nl per site) located 200, 400, 600 and 800 μm dorsal from the cranial floor. After > 14 days post-injection, mice were terminally anaesthetized using an intraperitoneal injection of a ketamine/domitor mixture (75 mg/kg ketamine, 1 mg/kg domitor) and transcardially perfused with 30 ml of phosphate-buffered saline (PBS) followed by 30 ml of 4% paraformaldehyde (PFA, Sigma-Aldrich,

MO, USA), dissolved in PBS and adjusted to pH 7.4. Brains were post-fixed at 4°C for 1–3 days in 4% PFA solution, then transferred to PBS solution. Individual brains were cut into coronal sections (60 μm) using a vibrating microtome (Leica VT1200S, Leica Microsystems (UK) Ltd.) and mounted with Vectashield Antifade Mounting Medium (Vector Laboratories, CA, USA). Images were acquired with a Leica DM R epifluorescence microscope and image analysis was performed using ImageJ (Rueden et al., 2017) and MATLAB (MathWorks, MA, USA). To obtain estimates of the depth of layer 5B in CFA, 3 coronal sections from each brain were imaged (0.54 mm, 0.6 mm and 0.66 mm rostral to bregma). Brightness/contrast adjustments and background subtraction (rolling ball, 30 pixels wide at 1.28 μm/pixel; Fiji (Schindelin et al., 2012)) functions were performed to reduce the contribution of background autofluorescence. Each ROI was then divided into 25 μm deep bins that were normalized to a value between 0 and 1, with 0 being the darkest bin and 1 being the brightest bin and all bins were compared to baseline. To obtain a depth profile of layer 5B within CFA, the depth of the dorsal-most retrogradely labeled neurons were recorded at 100 μm intervals from 1.3 - 1.9 mm lateral to bregma and repeated in 5 sequential coronal sections from 0.36 - 0.84 mm rostral to bregma. For each mouse, the depth of layer 5B at the center of CFA (1.6 mm lateral, 0.6 mm rostral to bregma) was taken as the reference depth and the depths of other locations reported relative to this value.

Immunohistochemistry

Mice expressing GCaMP6s were transcardially perfused and horizontal sections (30 μm) were cut parallel to the surface of CFA. Sections were rinsed in PBS overnight, incubated with a blocking solution (PBS, with 0.5% Triton X-100 (Sigma-Aldrich) and 10% goat serum (Sigma-Aldrich)) for 2 hrs and rinsed with PBS. Sections were incubated overnight with mouse anti-NeuN (MAB377 Anti-NeuN Antibody, clone A60, Sigma-Aldrich) diluted 1:1500 in carrier solution (PBS, with 0.5% Triton X-100 and 1% goat serum), then rinsed with PBS. For secondary antibody binding, sections were incubated overnight with goat anti-mouse Alexa Fluor 568 (Invitrogen, MA, USA) diluted 1:750 in carrier solution then rinsed with PBS. Sections were mounted onto glass slides, briefly air-dried, covered with Vectashield Antifade Mounting Medium (Vector Laboratories), and sealed with a glass coverslip. Images of CFA were acquired using a Nikon A1R FLIM confocal microscope (20X objective lens, 0.8 NA, Plan Apo VC, Nikon, Europe). Three images were taken at imaging planes corresponding to layer 5B (550 μm from the cortical surface). The number of cells in each image was manually counted and divided by the area to obtain a measure of neuron density. For most FOVs recorded during calcium imaging, neurons were not visible in all portions of the frame due to occlusion by blood vessels. Polygons were manually drawn around visible neurons in each field-of-view to provide a realistic estimate of the imaging area.

2-photon imaging

To perform population calcium imaging in layer 5B (12 FOVs, N = 6 mice), 200 nl of the adeno-associated virus (AAV) AAV1-SynGCaMP6s (diluted to $2.9x10^{12}$ GC/ml, Addgene 100844-AAV1) was injected into CFA (1.6 mm lateral, 0.6 mm rostral to bregma and 0.6 mm from the cortical surface) using a pulled glass pipette (5 μl, Drummond Scientific; 10–20 nl/min) and automated injection system (Model Picospritzer iii, Parker), before sealing the craniotomy with silicone (Body Double; Smooth-On, PA, USA) and implanting a lightweight headplate. For imaging, a cranial window (glass coverslip #0; Menzel-Gläser, Germany fixed with cyanoacrylate glue), was implanted above the virus injection site. 2-photon calcium imaging was performed using a custom-built resonant scanning 2-photon microscope (320 x 320 μm FOV; 600 x 600 pixels) with a Ti:Sapphire pulsed laser (Chameleon Vision-S, Coherent, CA, USA; < 75 fs pulse width, 80 MHz repetition rate) tuned to 920 nm wavelength. Images were acquired at 40 Hz with a 40x objective lens (0.8 NA; Nikon) and custom-programmed LabVIEW-based software (LotoScan).

For cell type specific imaging, AAV-pkg-Cre (Addgene 24593-AAVrg; $1.7x10^{13}$ GC/ml) was injected into either the ipsilateral (right) pons (PT; 0.4 mm lateral, 0.4 mm rostral to lambda and 0.2, 0.4 and 0.6 mm dorsal from the cranial floor) or contralateral (left) CFA (IT; 4 injections centered on 1.6 mm lateral, 0.6 mm rostral relative to bregma at 0.7 and 0.35 mm from the cortical surface) followed by an injection of pAAV-CAG-Flex-mRuby2-GSG-P2A-GCaMP6s-WPRE-pA (Addgene 68717-AAV1; $1.8x10^{13}$ GC/ml) into right CFA (1.6 mm lateral, 0.6 mm rostral to bregma and 0.6 mm from the cortical surface). 2-photon calcium imaging was performed using an 8 kHz resonant scanning microscope (HyperScope, Scientifica, UK; 690 x 690 μm FOV; 512 x 512 pixels) with a Ti:Sapphire pulsed laser (Chameleon Vision-S, Coherent, CA, USA; < 75 fs pulse width, 80 MHz repetition rate) tuned to 920 nm. Images were acquired at ~30 Hz with a 16x objective lens (0.8 NA; Nikon) using SciScan image software (Scientifica) and synchronized with external high-speed videos and behavioral data using Mantis64. To facilitate reliable imaging at depths > 500 μm, all imaging was performed 24 hrs post-surgery. Laser power was between 91 – 173 mW (mean = 143 mW) across all imaging sessions, well below the damage thresholds of 250 – 300 mW outlined in Podgorski and Ranganathan (2016). The combination of low pixel dwell time and systematic blanking of FOV edges, where the dwell time is higher, and the addition of room temperature artificial cerebrospinal fluid on the surface of the skull reduced the risk of thermal effects (as discussed in Podgorski and Ranganathan 2016).

Motion artifacts in the raw fluorescence videos were corrected using discrete Fourier 2-dimensional-based image alignment (SIMA 1.3.2; (Kaifosh et al., 2014)). ROIs were drawn manually in Fiji and pixel intensity within each ROI averaged to produce a raw fluorescence time series (F). To remove fluorescence originating from neuropil and neighboring neurons, fluorescence signals were decontaminated and extracted using nonnegative matrix factorization, as implemented in FISSA (Keemink et al., 2018). Normalized fluorescence was calculated as $\Delta F/F_0$, where F_0 was calculated as the 5^{th} percentile of the 1 Hz low-pass filtered raw fluorescence signal and $\Delta F = F\text{-}F_0$. All further analyses were performed in custom written scripts in MATLAB or Python 3.

To identify movement-related neurons, we defined a baseline (-500 ms to -150 ms relative to motion index onset) and peri-movement (-150 ms relative to motion index onset to 40 ms after median movement completion) epoch. Next, we used two independent methods: 1) a bootstrapped distribution (10,000 samples) of baseline-to-peak values (mean of the 100 ms centered on the largest deviation from baseline within the peri-movement epoch - mean of baseline epoch) was used to test whether 95% confidence intervals were different from 0; 2) bootstrapped distributions of mean $\Delta F/F_0$ in 250 ms bins within the peri-movement epoch were compared to bootstrapped distributions of mean $\Delta F/F_0$ within the baseline epoch. If either method identified significant differences the neuron was classified as movement-related. Neurons with no differences between baseline and movement epochs were classified as non-responsive and excluded from further analysis. Neurons with a median onset occurring after median movement completion (plus a small correction factor of 40 ms, to account for the rise time of GCaMP6s) were defined as 'reward phase' neurons and excluded from further analysis. The median onset time of each cell was calculated by employing a previously published onset detection algorithm using a slope sum function (SSF; Zong et al., 2003; Dacre et al., 2021) with the decision rule and window of the SSF adapted to the calcium imaging data (threshold 10% of peak, SSF window 375 ms, smoothed with a Savitzky Golay filter across 27 frames with order 2 and reported as the median of 10,000 bootstrapped samples to reduce the influence of noisy individual trials). Prior to extracting $\Delta F/F_0$ onsets, we verified this algorithm with simulated data thereby accounting for any bias in the onset detection potentially introduced by filtering and/or the decision rule. To simulate the rising phase of the movement related calcium events in our data we used linear ramps with defined onset times and a rise time of 0.5 s mimicking GCaMP6s kinetics. We then calibrated the onset detection algorithm on the simulated data (100 simulated cells with 30 simulated trials per cell and artificially added noise in each trial matching the noise level in the imaging data) and updated it by a small correction factor. Neurons with movement bias were detected using the same classification criteria described above but across movements (i.e. significant differences in bootstrapped $\Delta F/F_0$ baseline-to-peak or 250 ms peri-movement bins).

Trial-to-trial correlations

To assess the similarity of trial-to-trial activity, the average pairwise trial-to-trial correlation coefficients (Pearson's r) of the peri-movement $\Delta F/F_0$, smoothed with a 1 s LOESS filter, were computed for each neuron. Data are presented as bootstrapped medians per animal for each movement bias classification (10,000 repetitions, 50 samples). To investigate the relationship between trial-to-trial similarity of movement and population $\Delta F/F_0$, pairwise trial-to-trial correlation coefficients (Pearson's r) of peri-movement motion index and pairwise trial-to-trial correlation coefficients (Pearson's r) of the peri-movement population $\Delta F/F_0$ of the same trials were compared. Population $\Delta F/F_0$ was the sum of all movement-related neurons in each FOV. Data were binned according to the pairwise trial-to-trial correlation coefficients of their motion index and are presented as the bootstrapped median (10,000 repetitions, 50 samples) within each bin.

Extracellular recording and spike sorting

To compare neural activity during the task, extracellular unit recordings in CFA were performed using acutely implanted silicone probes (Neuropixels 1.0 probes, IMEC). Data were acquired from the 384 channels closest to the probe tip (bank 0) with SpikeGLX software at 30 KHz, an amplifier gain of 500 for each channel and high-pass filtered with a cutoff frequency of 300 Hz. Spike data were synchronized with external high-speed videos and behavioral data (cue presentation, lever movement, and reward delivery) using Mantis64. Spike sorting was performed using Kilosort3 to automatically cluster units from raw data (Pachitariu et al., 2016). The resulting spike clusters were manually curated using Phy (https://github.com/cortex-lab/phy), and any unit with sufficient refractory period violations, inconsistent waveform amplitude across the duration of the recording, or clipped amplitude distribution was excluded from analyses. Probe location was confirmed via DiI (Thermofisher) reconstruction of the recording track and compared to retrogradely labeled PT neurons (FastBlue (Polysciences) injected into the pons) in each animal to limit analysis to units within layer 5B (upper boundary, 500-680 μm; lower boundary, 900-1080 μm; N = 5 mice). Spike widths were calculated as the duration from trough to following maxima of the spike waveform. Putative pyramidal neurons were identified as units with median spike widths greater than 0.4 ms.

To classify units as responsive to push or pull movements, firing rates were calculated by convolving motion index-aligned spike times with a 50 ms Gaussian kernel and mean changes in firing rate were calculated by subtracting the mean firing rate during a baseline period (1 s period before cue presentation) from the mean firing rates in 250 ms bins tiling a response period extending back from *max*(*pX ushcompletion*,*pX* u*llcompletion*)) to include motion index onset. Briefly, motion index onsets were calculated as the first point after cue where the motion index was > threshold (threshold = mean motion index in a baseline window from the 1.5 s before cue plus 2 SD). Trials where the motion index onset was prior to cue presentation were excluded from analysis. Significant responses were identified by comparing bootstrapped 95% confidence intervals of mean changes in firing rates to 0; if at least one bin differed from 0, that unit is considered movement-responsive. Movement-responsive units were classified as having a push or pull bias if confidence intervals did not overlap.

Neural decoding

To decode movement type in single neurons we employed a naïve Bayes classifier, where distributions of features are assumed to be Gaussian. Movement-aligned $\Delta F/F_0$ data were assessed within a 5 s peri-movement window to produce a time series for the decoding accuracy. At each time point, leaving one trial out (test trial), the likelihood of determining a push or pull was esti-

mated based on the remaining trials (training set). The leave-one-out procedure was then repeated for all trials to calculate a mean decoding accuracy time series for each neuron. The resulting time series were analyzed within the peri-movement epoch - the peri-movement epoch began at -0.15 s relative to motion index onset and ended based on the peak $\Delta F/F_0$ response of each neuron; the position of the median peak was calculated for each movement type and the later of these time points used as the cut off. To identify neurons with decoding performance above chance, the bootstrapped distributions of decoding accuracy scores were compared against a threshold value for each session. Only neurons with at least 1 bin significantly higher than threshold were defined as high decoding accuracy. The threshold for each session was calculated based on modeled data composed of random samples from a Gaussian distribution with the same number of trials as the experimental data. For each session, modeled data accuracy was calculated 1000 times, assuming a prior probability of 50:50, and the mean + 2 SD was used as the threshold for significance. For population level classification of movement type, we employed logistic regression. As above, the decoding accuracy of the time series for each population was generated via leave-one-out design looped over all the trials in a given session. Population decoding accuracy was defined as the maximum decoding accuracy in any 250 ms bin within the peri-movement epoch. Population decoding was also performed on subsets of the entire population. Neurons were removed from the population one at a time, either in order from highest to lowest decoding accuracy score or randomly, with the network retrained for each iteration. The process was repeated 25 times in the random condition and the median of all responses used as the representative example for comparison with the ordered removal condition. Subpopulations of neurons decoding significantly above chance were determined by comparing decoding scores with a shuffled dataset (sampled randomly from 1000 time points with the trial labels (push or pull) randomized for each sample). If confidence intervals from the population data did not overlap with those of the shuffled data, population scores were deemed to be above chance. In 3/12 FOVs the number of high decoding accuracy neurons and/or trial number were low and were excluded from further comparison.

Dimensionality reduction

Raw fluorescence traces for all trials with successful movements in a 7.5 s peri-movement window were concatenated, filtered with a three frame (75 ms) wide boxcar kernel, whitened, and transformed with principal component analysis. The principal components (PCs) corresponding to the 16 highest eigenvalues, which corresponded to an average 83% (range [77 94]) cumulative explained variance, were analyzed. To compute trajectories in PC space, PC projections for all trials were averaged (separately for push or pull) and the variance and 95% confidence intervals for each time point estimated via 100-fold bootstrapping. The separability of the trajectories for push or pull was computed in each PC separately as $d'(t) = |mpush(t) - m_{pull}(t)| / \sqrt{0.5(v_{push}(t) + v_{pull}(t))}$, where $m_{push}(t)$ and $m_{pull}(t)$ are the mean trajectories for push and pull, and $v_{push}(t)$ and $v_{pull}(t)$ the corresponding variances, estimated from trials. The separability $d'(t)$ was bootstrapped from 400 samples, and variance and 95% confidence intervals estimated from this sample. $d'(t)$ was computed for all frames from movement onset to completion, where the latter was the longest movement duration recorded in each session. PCs were considered separable if the difference between d'(t) and $d_{shuffle}'(t)$ (obtained in the same way from trial-shuffled data) was within the 95% confidence interval, which was estimated from the sum of the relevant bootstrapped variances. For each FOV, the largest significant $d'(t)$ was used; in 1/12 FOVs no PCs showed significant separability and was excluded.

Spatiotemporal mapping

To assess the functional (temporal) organization of simultaneously recorded populations of neurons, pairwise correlation coefficients (Pearson's r) from the smoothed (1 s LOESS filter) and motion index-aligned $\Delta F/F_0$ within the peri-movement epoch were compared. Data were split based on their decoding accuracy scores and the bootstrapped median difference between high decoding accuracy neurons and those of the population were subtracted and a median difference calculated per sample. This process was repeated 10,000 times to generate a distribution for high decoding neurons versus the entire population and the same sampling procedure was used to investigate the correlations within low decoding accuracy neurons. To investigate spatial clustering, bootstrapped median differences between high decoding accuracy neurons and the population using pairwise distances (defined as the Euclidean distance between the centroids of manually drawn ROIs from 2-photon imaging processing) were compared. A Generalized Linear Mixed-Effects Model:

$$r \sim distance_{pairwise} \times accuracy_{decoder} + movement_{type} + animal$$

was used to model the pairwise correlation coefficient as a function of pairwise distance (continuous), decoding accuracy and movement type. Pairwise distance and decoding accuracy were modeled as interacting fixed terms, while movement type and animal were modeled as random intercepts to account for the dependency of the measurements on observations from the same animal and across the different movement types. The model was estimated using the restricted maximum likelihood, or REML, method (Bartlett and Fowler, 1937). Model assumptions were verified by comparing residual versus fitted values for each covariate in the model against each covariate removed from the model.

QUANTIFICATION AND STATISTICAL ANALYSIS

Data analysis was performed using custom-written scripts in MATLAB or Python3 and code will be made available on request. All statistical details of experiments can be found in the figure legends or main text, including description of the specific test used and sample sizes. Data are reported as mean ± 95% bootstrapped confidence interval, 10,000 bootstrap samples, unless otherwise indicated. Where multiple measurements were made from a single animal, suitable weights were used to evaluate summary population statistics. Statistical significance was considered when $p < 0.05$ unless otherwise stated. Data were tested for normality and parametric/non-parametric tests were used as appropriate and as detailed in the text. The GLMM was designed in Python using the statsmodels library (Seabold and Perktold, 2010).

Cell Reports, Volume *39*

Supplemental information

Movement-specific signaling is differentially distributed across motor cortex layer 5 projection neuron classes

Stephen P. Currie, Julian J. Ammer, Brian Premchand, Joshua Dacre, Yufei Wu, Constantinos Eleftheriou, Matt Colligan, Thomas Clarke, Leah Mitchell, A. Aldo Faisal, Matthias H. Hennig, and Ian Duguid

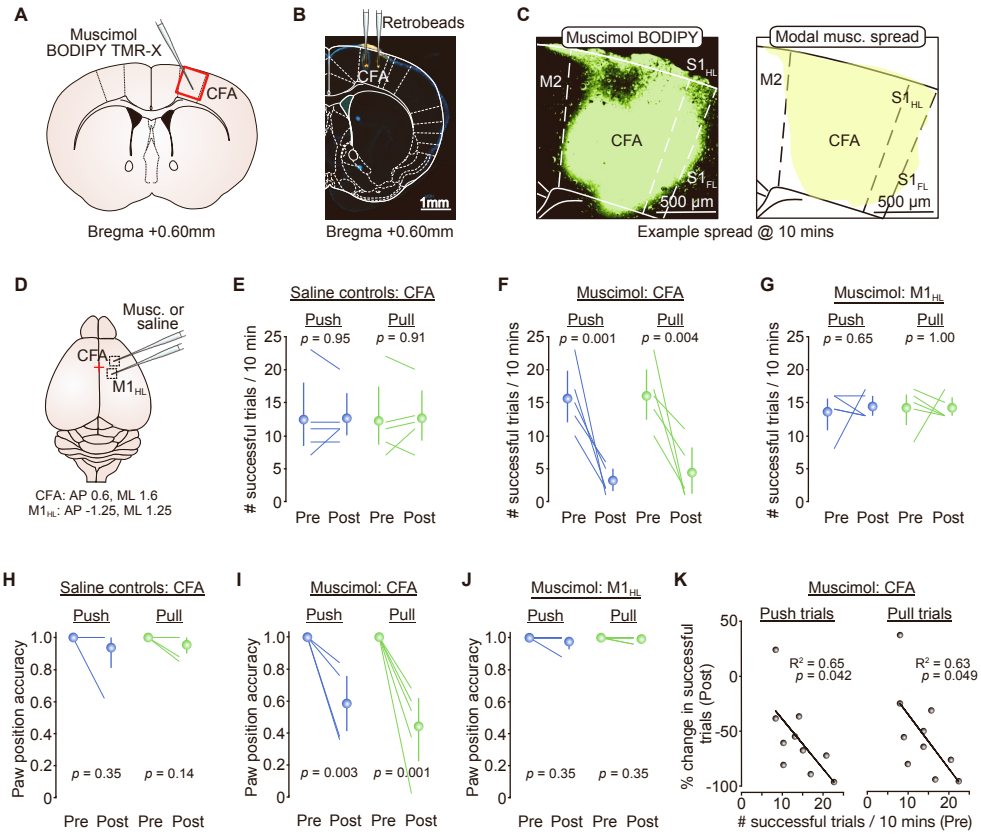

Figure S1 - Muscimol inactivation of CFA affects forelimb posture and task success. Related to Figure 1.

(A) Injection of muscimol BODIPY TMR-X into caudal forelimb area (CFA).
(B) Muscimol injection sites visualized using fluorescent retrobeads.
(C) *Left*, example image of fluorescent muscimol spread in CFA at 10 mins post injection. *Right*, modal spread of fluorescent muscimol in CFA (i.e., area in which fluorescence is present across all mice) (N = 3 mice). M2, secondary motor cortex; $S1_{HL}$, hindlimb primary somatosensory cortex; $S1_{FL}$, forelimb primary somatosensory cortex.
(D) Focal muscimol inactivation of CFA or hindlimb motor cortex ($M1_{HL}$), 0.6 mm anterior, 1.6 mm lateral of bregma and 1.25 mm posterior, 1.25 mm lateral of bregma, respectively. Red cross denotes bregma.
(E-G) Number of successful push (blue) and pull (green) trials in a 10 min period before (Pre) and after (Post) injection of (E) saline into CFA, (F) muscimol into CFA or (G) muscimol into $M1_{HL}$ (N = 5 mice), paired t-test. Colored lines, individual mice. Symbols, population means ± 95% CI.
(H-J) Paw position accuracy at the point of cue presentation before (Pre) and 10 mins after (Post) (H) saline into CFA, (I) muscimol into CFA or (J) muscimol into $M1_{HL}$ (N = 5 mice), paired t-test. Colored lines, individual mice. Symbols, population means ± 95% CI.
(K) Correlation between the number of successful push (left) and pull (right) trials before (Pre) and the % change in successful trials after (Post) muscimol injection (N = 10 mice). Symbols, individual animals, Black line, linear fit to the data (Pearson's *r*).

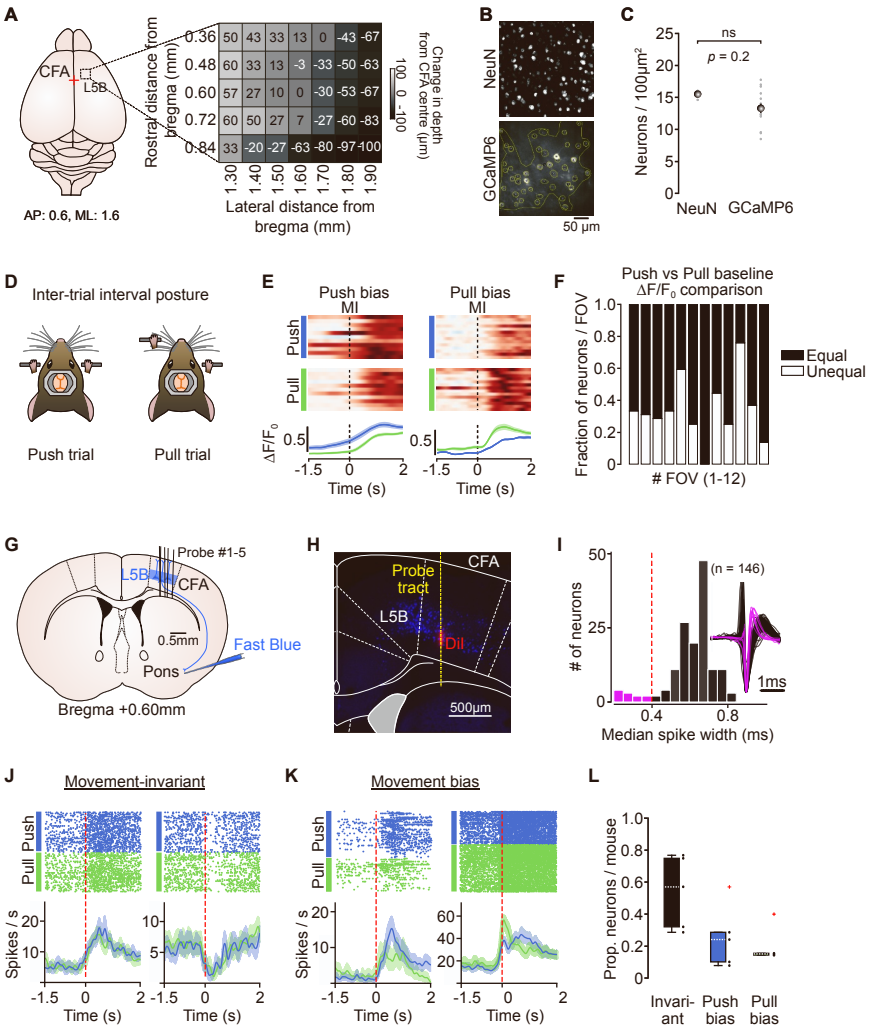

Figure S2 - Cell density and movement-type classification in layer 5B of CFA. Related to Figure 2.

(A) *Left*, schematic showing mapped region of caudal forelimb area (CFA) centred on 0.6 mm anterior, 1.6 mm medial of bregma. Red cross denotes bregma; *Right*, heatmap indicating changes in layer 5B depth across a range of cortical coordinates. Values represent the mean depth in µm of the upper boundary of Layer 5B (N = 3 mice).
(B) *Top*, representative image of NeuN stained layer 5B neurons; *Bottom*, representative two-photon FOV of L5B neurons expressing GCaMP6s. Small circles depict regions-of-interest (yellow) drawn around individual neurons within a larger bounded area excluding blood vessels.
(C) Average number of NeuN versus GCaMP6s expressing neurons / 100µm^2 in layer 5B of CFA. Gray dots represent individual slices, bars depict s.e.m. (NeuN, n = 3 slices, N = 1 mouse; GCaMP6s, n = 15 slices, N = 7 mice; two-sample t-test).
(D) Schematic depicting inter-trial posture for push (left) and pull (right) trials.
(E) Activity of two neurons with differences in inter-trial baseline $\Delta F/F_0$. *Left*, example neuron with push bias. *Right*, example neuron with pull bias. *Top*, raster showing normalized $\Delta F/F_0$ across successive push (blue) or pull (green) trials; *Bottom*, mean $\Delta F/F_0$ ± 95% CI for push and pull trials. Dashed lines, movement initiation (MI).
(F) Proportion of neurons per field-of-view (FOV) with equal (black) or unequal (white) inter-trial $\Delta F/F_0$ baselines (n = 486 neurons from 12 FOVs, N = 6 mice).
(G) Silicone probe recordings of putative layer 5B (L5B) neurons in CFA. Approximate position of probes within CFA are shown. The upper and lower boundaries of layer 5B are defined based on retrograde labeling of pyramidal tract (PT) neurons after FastBlue injection into the pons (N = 5 mice).
(H) Retrograde labeling of pons-projecting PT neurons within CFA (blue) with silicon probe tract visualized using DiI (red). Dashed line, overlay of probe tract.
(I) Histogram of spike durations, highlighting putative interneurons (purple) and pyramidal neurons (black). Inset, trough-aligned mean spike waveforms, normalized based on peak-to-trough height (n = 148 units, N = 5 mice).
(J) Activity of two example movement-invariant layer 5 CFA neurons. *Top*, Spike rasters during push (blue) and pull (green) trials. Dots represent individual spikes. *Bottom*, peri-stimulus time histograms depicting mean ± s.e.m. firing rate during push (blue) and pull (green) trials. Red dashed lines, movement initiation (MI).
(K) Activity of two example layer 5 CFA neurons with push (left) and pull (right) bias. *Top*, Spike rasters during push (blue) and pull (green) trials. Dots represent individual spikes. *Bottom*, peri-stimulus time histograms depicting mean ± s.e.m. firing rate during push (blue) and pull (green) trials. Red dashed lines, movement initiation (MI).
(L) Proportion of invariant, push- and pull-bias neurons per mouse (n = 71 neurons, N = 5 mice). Black dots represent individual mice. Red crosses, identified outliers.

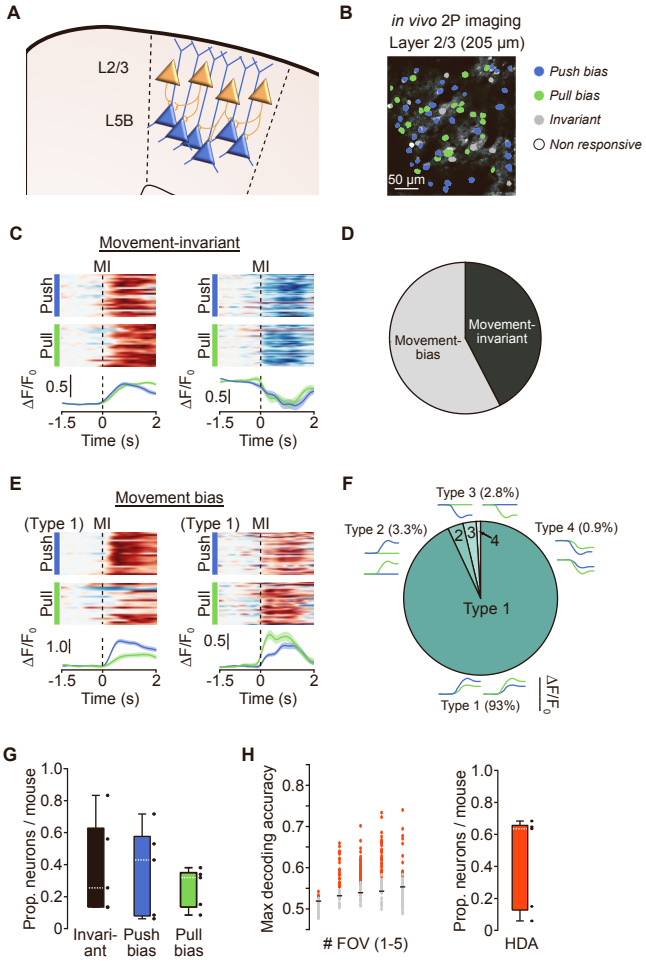

Figure S3 - Movement-specific signalling is more prevalent in Layer 2/3 neurons. Related to Figure 2 and Figure 3.

(A) Schematic showing top-down laminar inter-connectivity between layer 2/3 and layer 5B of CFA.
(B) Example FOV showing layer 2/3 CFA neurons with push (blue) or pull (green) bias. Gray, movement-invariant; white, non-responsive neurons.
(C) Activity of two example movement-invariant neurons. *Top*, raster showing normalised $\Delta F/F_0$ across successive push (blue) or pull (green) trials; *Bottom*, mean $\Delta F/F_0$ ± 95% CI for push and pull trials. Dashed lines, movement initiation (MI).
(D) Summary of movement-invariant and movement-bias neuron classification in CFA layer 2/3 neurons (n = 215 vs 160 neurons, N = 5 mice).
(E) Activity of two example Type 1 movement-bias neurons. *Top*, raster showing normalised $\Delta F/F_0$ across successive push (blue) or pull (green) trials; *Bottom*, mean $\Delta F/F_0$ ± 95% CI for push and pull trials. Dashed lines, movement initiation (MI).
(F) Summary of movement-bias classification in CFA layer 2/3 neurons (n = 215 neurons, N = 5 mice). *Insets*, model examples of $\Delta F/F_0$ changes classified as Type 1 - 4.
(G) Proportion of invariant, push- and pull-bias neurons per mouse (n = 375 neurons from 5 FOVs, N = 5 mice). Black dots represent individual mice.
(H) *Left*, maximum decoding accuracy during peri-movement epochs generated using a naïve Bayes classifier. Circles represent individual neurons; black horizontal lines indicate significance threshold. *Right*, box-and-whisker plot showing the proportion of high decoding accuracy (HDA) neurons across mice (n = 375 neurons from 5 FOVs, N = 5 mice).

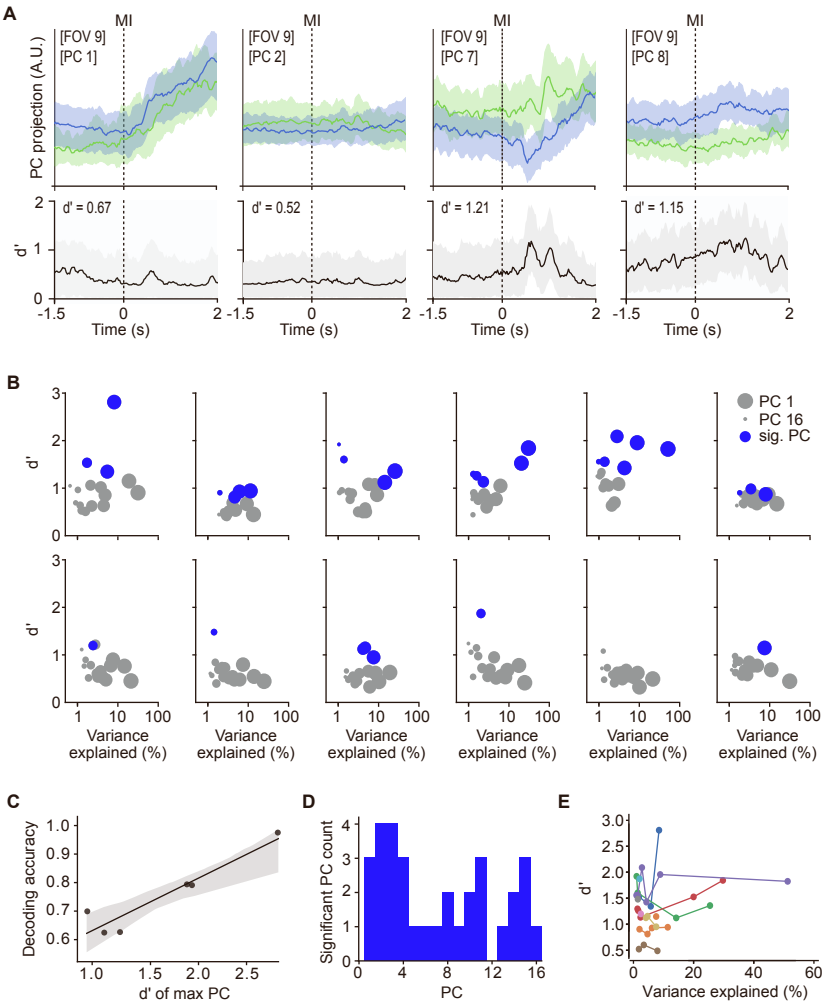

Figure S4 - Movement type is represented in both leading and higher principal components. Related to Figure 3.

(A) *Top*, example trajectories of 4 principal components (PC) from a representative field-of-view (FOV) during push (blue) and pull (green trials). *Bottom*, discrimination index (d') calculated from the corresponding PCs. Inset, maximum d' of each PC. Thick lines, mean ± 95% CI. Dashed lines, movement initiation (MI).
(B) Variance explained as a function of discrimination index (d') for all PCs in each FOV. *Top*, FOVs 1-6. *Bottom*, FOVs 7-12. Dot size (large to small) represents PC rank (1-16). Blue dots are significant PCs.
(C) Discrimination index (d') of the highest significant PC vs population decoding accuracy (Figure 3) for each mouse (N = 6 mice). Black line, linear regression fit ± 95% CI.
(D) Histogram of significant PCs across all 12 FOVs.
(E) Significance explained as a function of discrimination index (d') for all significant PCs. Dots represent individual PCs. Lines and colours link PCs from the same FOV.

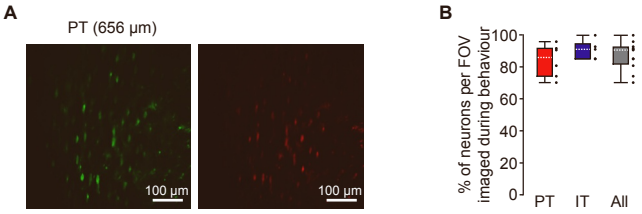

Figure S5 - Quantifying proportions of imaged neurons per field-of-view. Related to Figure 4.

(A) Example field-of-view (FOV) showing PT neurons expressing GCaMP6s (left; green) and mRuby (right; red).
(B) Percentage of mRuby positive PT and IT neurons per FOV imaged ($\Delta F/F_0$) during behaviour. Box-and-whisker plots showing median, interquartile range and range. PT (red), IT (purple) and all neurons (gray). Black dots represent individual FOVs. N = 6, 5 and 11, respectively.

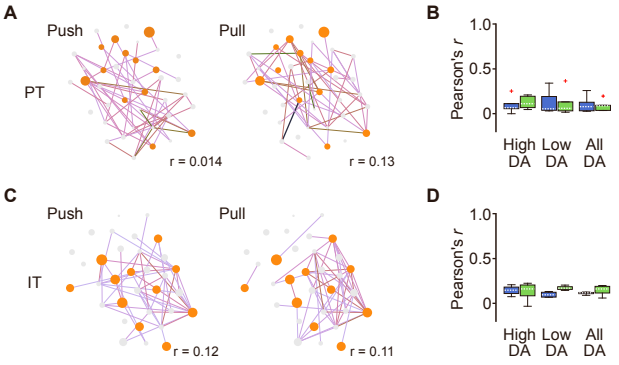

Figure S6 - Temporal organization of high decoding accuracy neurons in layer 5B during push and pull movements. Related to Figure 5.

(A) *Left & right*, functional networks constructed from the pairwise activity correlations from a representative PT field-of-view (FOV) for push (left) or pull (right) trials. Line color (light to dark) and width correspond to increasing values of Pearson's *r*. Neurons are plotted as nodes in Euclidean space with color and size relating to increasing decoding accuracy.
(B) Box-and-whisker plots showing the median, interquartile range and range of correlation coefficients across mice for high decoding accuracy (HDA), low decoding accuracy (LDA) and all neurons. Data are shown for both push (blue) and pull (green) trials. Red crosses, identified outliers.
(C) *Left & right*, functional networks constructed from the pairwise activity correlations from a representative IT FOV for push (left) or pull (right) trials. Line color (light to dark) and width correspond to increasing values of Pearson's *r*. Neurons are plotted as nodes in Euclidean space with color and size relating to increasing decoding accuracy.
(D) Box-and-whisker plots showing the median, interquartile range and range of correlation coefficients across mice for high decoding accuracy (HDA), low decoding accuracy (LDA) and all neurons. Data are shown for both push (blue) and pull (green) trials.

Table S1 - Contributions Matrix. Related to Figures 1-5 and Figures S1-S6.

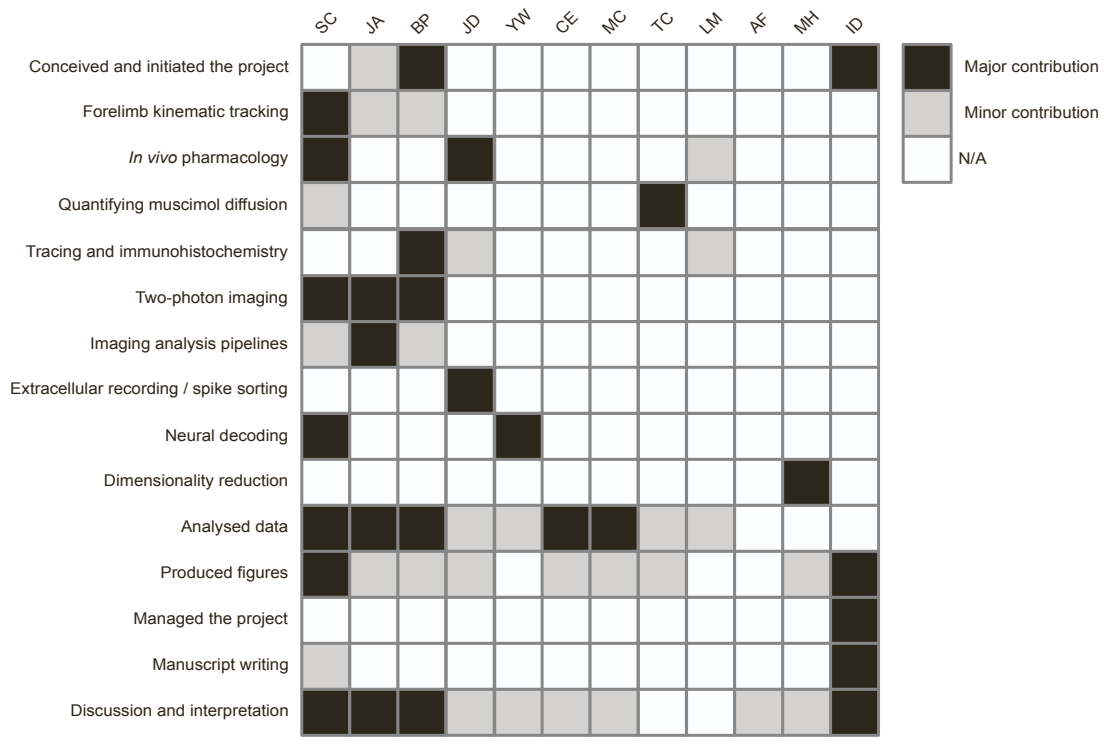

Table S2, statistical details, related to Figures 1-5 and Figures S1-S6.

$\bar{X}$ = mean $\tilde{X}$ = median SD = standard deviation IQR = interquartile range
fov = fields-of-view H / LDA = high / low decoding accuracy GLMM = generalised linear mixed-effects model

Figure	Description	Sample size	Result	Variance	Confidence intervals (95%)	Statistical test result
1C-E	Training time (days)	N = 24	$\tilde{X}$ = 10.5	IQR = 4		
1C	Reaction time (s; push / pull)	N = 24	$\tilde{X}$ = 0.132 / 0.135	IQR = 0.058 / 0.043		
	Movement duration (s; push / pull)	N = 24	$\tilde{X}$ = 706 / 422	IQR = 352 / 438		
1D	Successful trials / session (push / pull)	N = 24	$\tilde{X}$ = 44.5 / 45	IQR = 9.5 / 8.5		
1E	Task success (%; push / pull)	N = 24	$\tilde{X}$ = 68.0 / 74.5	IQR = 35.9 / 43.4		
1G	Successful trials / 10min (push muscimol CFA pre / post)	N = 10	$\bar{X}$ = 13.9 / 5	SD = 5.22 / 2.94	[11.1 17.1] / [3.3 6.8]	t(18) = 4.70, P = 1.79×10^{-4}, paired t-test
	Successful trials / 10min (pull muscimol CFA pre / post)	N = 10	$\bar{X}$ = 14.0 / 5.3	SD = 5.33 / 3.62	[10.9 17.2] / [3.2 7.4]	t(18) = 4.27, P = 4.64×10^{-4}, paired t-test
1H	Paw position accuracy (push muscimol CFA pre / post)	N = 10	$\bar{X}$ = 1 / 0.66	SD = 0 / 0.2	[1 1] / [0.54 0.77]	t(18) = 5.56, P = 2.79×10^{-5}, paired t-test
	Paw position accuracy (pull muscimol CFA pre / post)	N = 10	$\bar{X}$ = 0.98 / 0.50	SD = 0.06 / 0.21	[0.95 1] / [0.36 0.62]	t(18) = 6.85, P = 2.07×10^{-6}, paired t-test
S1. E	Successful trials / 10min (push saline CFA pre / post)	N = 5	$\bar{X}$ = 12.4 / 12.6	SD = 6.23 / 4.28	[8.6 18] / [10 16.4]	t(8) = -0.06, P = 0.95, paired t-test
	Successful trials / 10min (pull saline CFA pre / post)	N = 5	$\bar{X}$ = 12.2 / 12.6	SD = 5.81 / 4.72	[8.6 17.4] / [9 16.6]	t(8) = -0.12, P = 0.91, paired t-test

S1. F	Successful trials / 10min (push muscimol CFA pre / post)	N = 5	$\bar{X}$ = 15.6 / 3.2	SD = 4.88 / 2.17	[12.0 19.8] / [1.6 4.8]	t(8) = 5.19, $P = 8.29 \times 10^{-4}$, paired t-test
	Successful trials / 10min (pull muscimol CFA pre / post)	N = 5	$\bar{X}$ = 16.0 / 4.4	SD = 4.74 / 4.45	[12.4 20.0] / [1.2 8.2]	t(8) = 3.99, $P = 4.0 \times 10^{-3}$, paired t-test
S1. G	Successful trials / 10min (push muscimol $M1_{HL}$ pre / post)	N = 5	$\bar{X}$ = 13.6 / 14.4	SD = 3.29 / 1.95	[10.8 15.6] / [13.0 16.0]	t(8) = -0.47, $P = 0.65$, paired t-test
	Successful trials / 10min (pull muscimol $M1_{HL}$ pre / post)	N = 5	$\bar{X}$ = 14.2 / 14.2	SD = 3.11 / 1.79	[11.4 16.2] / [13.0 15.8]	t(8) = 0, $P = 1.0$, paired t-test
S1. H	Paw position accuracy (push saline CFA pre / post)	N = 5	$\bar{X}$ = 1 / 0.92	SD = 0 / 0.17	[1 1] / [0.77 1]	t(8) = 1.0, $P = 0.35$, paired t-test
	Paw position accuracy (pull saline CFA pre / post)	N = 5	$\bar{X}$ = 1 / 0.95	SD = 0 / 0.07	[1 1] / [0.89 1]	t(8) = 1.62, $P = 0.15$, paired t-test
S1. I	Paw position accuracy (push muscimol CFA pre / post)	N = 5	$\bar{X}$ = 1 / 0.59	SD = 0 / 0.22	[1 1] / [0.41 0.76]	t(8) = 4.27, $P = 2.7 \times 10^{-3}$, paired t-test
	Paw position accuracy (pull muscimol CFA pre / post)	N = 5	$\bar{X}$ = 1 / 0.44	SD = 0 / 0.26	[1 1] / [0.23 0.62]	t(8) = 4.79, $P = 1.4 \times 10^{-3}$, paired t-test
S1. J	Paw position accuracy (push muscimol $M1_{HL}$ pre / post)	N = 5	$\bar{X}$ = 1 / 0.98	SD = 0 / 0.05	[1 1] / [0.93 1]	1(8) = 1.0, $P = 0.35$, paired t-test
	Paw position accuracy (pull muscimol $M1_{HL}$ pre / post)	N = 5	$\bar{X}$ = 1 / 0.99	SD = 0 / 0.02	[1 1] / [0.98 1]	1(8) = 1.0, $P = 0.35$, paired t-test
S1. K	Successful trial vs % change in successful trials (push / pull)	N = 10				$r^2 = -0.65$ $P = 0.042$ / $r^2 = -0.63$, $P = 0.049$
2D	Prop. of responsive neurons (non / movement / reward)	N = 6 fov = 12 cell = 653	$\bar{X}$ = 20.9 / 73.5 / 5.7	SD = 15.1 / 16.0 / 3.7	[12.8 29.1] / [64.7 81.8] / [3.7 7.7]	

2E	Trial-trial correlation - ΔF/F0 vs motion index for push trials (motion index correlation 0.1 / 0.3 / 0.5 0.7)	N = 6 fov = 12 trials = 2931	$\tilde{X}$ = 0.36 / 0.62 / 0.75 / 0.80		[0.24 0.40] / [0.46 0.68] / [0.60 0.86] / [0.65 0.89]	
	Trial-trial correlation - ΔF/F0 vs motion index for pull trials (motion index correlation 0.1 / 0.3 / 0.5 0.7)	N = 6 fov = 12 trials = 2931	$\tilde{X}$ = 0.25 / 0.47 / 0.59 / 0.79		[0.23 0.27] / [0.37 0.87] / [0.52 0.68] / [0.65 0.89]	
2G	# of movement-responsive neurons (%; bias / invariant)	N = 6 fov = 12 Cell = 468	181 (38.7) / 287 (61.3)			
2J	# of movement bias neurons (%; type 1 / 2 / 3 / 4)	N = 6 fov = 12 Cell = 181	136 (75.1) / 25 (13.8) / 15 (8.3) / 5 (2.8)			
2L	Average ΔF/F0 trial-trial correlation for push trials (non / push / push)	N = 6 fov = 12 cell = 468	$\tilde{X}$ = 0.37 / 0.49 / 0.45	IQR = 0.37 / 0.47 / 0.39	[0.12 0.56] / [0.21 0.72] / [0.04 0.70]	
	Average ΔF/F0 trial-trial correlation for pull trials (non / push / push)	N = 6 fov = 12 cell = 468	$\tilde{X}$ = 0.31 / 0.30 / 0.53	IQR = 0.25 / 0.32 / 0.33	[0.10 0.65] / [0.08 0.75] / [0.06 0.61]	
2M	Prop. of movement-responsive neurons (non / push / pull)	N = 6 fov = 12 cell = 468	$\tilde{X}$ = 59.8 / 14.3 / 11.8	IQR = 31.4 / 15.9 / 19.5		
S2. C	Neurons / 100 μm^2 (NeuN / GCaMP6s)	N = 1 / 7 fov = 3 / 15	$\bar{X}$ = 15.6 / 13.3	SD = 0.9 / 2.7		t(16) = 1.75, P = 0.2, Student's t-test
S2. E-F	Prop. of biased neurons (equal / unequal baseline)	N = 6 fov = 12 cell = 181	$\tilde{X}$ = 69.5 / 30.5	IQR = 8.2 / 8.2		
S2. G-L	# units (%; pyramidal / interneurons)	N = 5 n = 146	137 (93.8) / 9 (6.2)			

	# units (%; non / move / reward)	N = 5 n = 137	61 (45.2) / 72 (52.6) / 4 (2.9)			
S2. L	Prop. of movement-responsive neurons (non / push / pull)	N = 5 n = 72	$\tilde{X}$ = 0.57 / 0.15 / 0.24	IQR = 0.43 / 0.01 / 0.19		
S3. D	# of movement-responsive neurons L2-3 (%; bias / invariant)	N = 5 fov = 5 cell = 375	216 (57.6) / 159 (42.4)			
S3. F	# of movement bias neurons L2-3 (%; type 1 / 2 / 3 / 4)	N = 5 fov = 5 cell = 216	200 (93.0) / 7 (3.3) / 6 (2.8) / 2 (0.9)			
S3. G	Prop. of movement-responsive neurons L2-3 (non / push / pull)	N = 5 fov = 5 cell = 375	$\tilde{X}$ = 0.25 / 0.43 / 0.32	IQR = 0.50 / 0.50 / 0.22		
S3. H	Prop. of movement-responsive neurons L2-3	N = 5 fov = 5 cell = 375	$\tilde{X}$ = 0.64	IQR = 0.53		
3A	Prop. of movement-responsive neurons (LDA / HDA)	N = 6 fov = 12 cell = 468	0.63 / 0.37			
3B	Decoding accuracy (single cell / population)	N = 6 fov = 12	$\tilde{X}$ = 0.61 / 0.75	IQR = 0.07 / 0.16		W = 1, Z = -2.20, P = 2.8×10^{-2}, Wilcoxon signed rank test
3F	Prop. neurons removed (high-low / random)	N = 6 fov = 9	$\tilde{X}$ = 0.21 / 0.64	IQR = 0.5 / 0.57		W = 1, Z = -2.20, P = 2.8×10^{-2}, Wilcoxon signed rank test
S4. C	Population decoding vs max d’	N = 6 fov = 10				r^2 =0.88, F(1,5) = 29.95, P = 5.4×10^{-3}

4E	# of movement-responsive neurons PT (%; bias / invariant)	N = 5 fov = 6 cell = 171	46 (26.9) / 125 (73.1)			
	# of movement bias neurons PT (%; type 1 / 2 / 3 / 4)	N = 5 fov = 6 cell = 46	36 (78.2) / 9 (19.6) / 1 (2.2) / 0 (0)			
	Prop. of movement-responsive neurons PT (non / push / pull)	N = 5 fov = 6 cell = 171	$\tilde{X}$ = 0.75 / 0.10 / 0.14	IQR = 0.21 / 0.19 / 0.11		
4G	# of movement-responsive neurons IT (%; bias / invariant)	N = 4 fov = 5 cell = 110	54 (49.1) / 56 (50.9)			
	# of movement bias neurons IT (%; type 1 / 2 / 3 / 4)	N = 4 fov = 5 cell = 54	34 (62.9) / 15 (27.8) / 2 (3.7) / 3 (5.6)			
	Prop. of movement-responsive neurons IT (non / push / pull)	N = 4 fov = 5 cell = 110	$\tilde{X}$ = 0.51 / 0.21 / 0.32	IQR = 0.11 / 0.26 / 0.31		
4I	Decoding accuracy PT (single / population) (HDA only)	N = 5 fov = 6 cell = 58	$\tilde{X}$ = 0.55 / 0.68	IQR = 0.02 / 0.14		t(4) = -3.04, P = 0.04
	Decoding accuracy IT (single / population) (HDA only)	N = 4 fov = 5 cell = 43	$\tilde{X}$ = 0.56 / 0.73	IQR = 0.04 / 0.21		t(3) = -2.95, P = 0.06
	Decoding accuracy population (PT / IT) (HDA only)	N = 5 / 4 fov = 6 / 5 cell = 58 / 43	$\tilde{X}$ = 0.68 / 0.73	IQR = 0.14 / 0.21		t(7) = 0.40, P = 0.70
S5. B	% of all neurons per FOV imaged during behaviour (PT / IT / All)	N = 5 / 4 / 9	$\tilde{X}$ = 85.8 / 91.2 / 90.7	IQR = 17.4 / 9.3 / 10.7		

		fov = 6 / 5 / 11				
5B	Norm. prop. $\Delta F/F_0$ onsets push PT (ms; HDA / LDA). ANOVA [animal:cell type: onset time]	N = 5 fov = 6 cell = 238	$\tilde{X}$ = 210 / 113	IQR = 709 / 662		F(4) = 0, P = 1 / F(1) = 0, P = 1 / F(17) = 5.12, $P = 8.32 \times 10^{-9}$
	Norm. prop. $\Delta F/F_0$ onsets pull PT (ms; HDA / LDA). ANOVA [animal:cell type: onset time]	N = 5 fov = 6 cell = 238	$\tilde{X}$ = 145 / 177	IQR = 226 / 500		F(3) = 0, P = 1 / F(1) = 0, P = 1 / F(17) = 8.57, $P = 3.35 \times 10^{-15}$
	Norm. prop. $\Delta F/F_0$ onsets push IT (ms; HDA / LDA). ANOVA [animal:cell type: onset time]	N = 4 fov = 5 cell = 137	$\tilde{X}$ = 500 / 339	IQR = 524 / 677		F(3) = 1.1×10^{-14}, P = 1 / F(1) = 0, P = 1 / F(17) = 7.31, $P = 4.85 \times 10^{-12}$
	Norm. prop. $\Delta F/F_0$ onsets pull IT (ms; HDA / LDA). ANOVA [animal:cell type: onset time]	N = 4 fov = 5 cell = 137	$\tilde{X}$ = 403 / 468	IQR = 444 / 710		F(3) = 0, P = 1 / F(1) = 0, P = 1 / F(17) = 3.81, $P = 6.85 \times 10^{-6}$
5D	Pairwise correlation coefficient PT (r; push; HDA vs ALL / LDA vs ALL)	N = 5 fov = 6 cell = 171	HDA $\tilde{X}$ = 0.07 LDA $\tilde{X}$ = 0.06 ALL $\tilde{X}$ = 0.08	HDA IQR = 0.05 LDA IQR = 0.16 ALL IQR = 0.10	[-0.103 0.087] / [-0.085 0.094]	P = 0.84 / 1.0
	Pairwise correlation coefficient IT (r; push; HDA vs ALL / LDA vs ALL)	N = 4 fov = 5 cell = 110	HDA $\tilde{X}$ = 0.15 LDA $\tilde{X}$ = 0.09 ALL $\tilde{X}$ = 0.12	HDA IQR = 0.07 LDA IQR = 0.05 ALL IQR = 0.01	[-0.093 0.081] / [-0.073 0.076]	P = 1.0 / 0.96
5E	Pairwise corr. Vs distance PT (HDA / LDA)	N = 5 fov = 6 cell = 171	Spearman r = -0.1 / 0.0			P = 0.87 / 1.0
	GLMM PT r distance pairwise accuracydecoder + movementtype+animal	N = 5, n = 3024 observations				P = 0.33
	Pairwise corr. Vs distance IT (HDA / LDA)	N = 4 fov = 5	Spearman r = -0.40 / 0.0			P = 0.6 / 1.0

		cell = 110				
	GLMM IT r distance pairwise accuracydecoder + movementtype+animal	N = 5, n = 1562 observations				*P* = 0.49
5G	Pairwise distance PT (µm; HDA vs ALL / LDA vs ALL)	N = 5 fov = 6 cell = 171	HDA $\tilde{X}$ = 226 LDA $\tilde{X}$ = 273 ALL $\tilde{X}$ = 264	HDA IQR = 26 LDA IQR = 60 ALL IQR = 53	[-69 102] / [-62 69]	*P* = 1.0 / 1.0
	Pairwise distance IT (µm; HDA vs ALL / LDA vs ALL)	N = 4 fov = 5 cell = 110	HDA $\tilde{X}$ = 228 LDA $\tilde{X}$ = 220 ALL $\tilde{X}$ = 229	HDA IQR = 14 LDA IQR = 56 ALL IQR = 58	[-82 67] / [-63 68]	*P* = 0.88 / 1.0
S6. B	Pairwise correlation coefficient PT (r; pull; HDA vs ALL / LDA vs ALL)	N = 5 fov = 6 cell = 171	HDA $\tilde{X}$ = 0.11 LDA $\tilde{X}$ = 0.06 ALL $\tilde{X}$ = 0.09	HDA IQR = 0.12 LDA IQR = 0.10 ALL IQR = 0.06	[-0.1 0.15] / [-0.1 0.09]	*P* = 1.17 / 0.79
S6. D	Pairwise correlation coefficient IT (r; pull; HDA vs ALL / LDA vs ALL)	N = 4 fov = 5 cell = 110	HDA $\tilde{X}$ = 0.16 LDA $\tilde{X}$ = 0.17 ALL $\tilde{X}$ = 0.16	HDA IQR = 0.12 LDA IQR = 0.03 ALL IQR = 0.08	[-0.08 0.07] / [-0.07 0.1]	*P* = 0.89 / 1.28